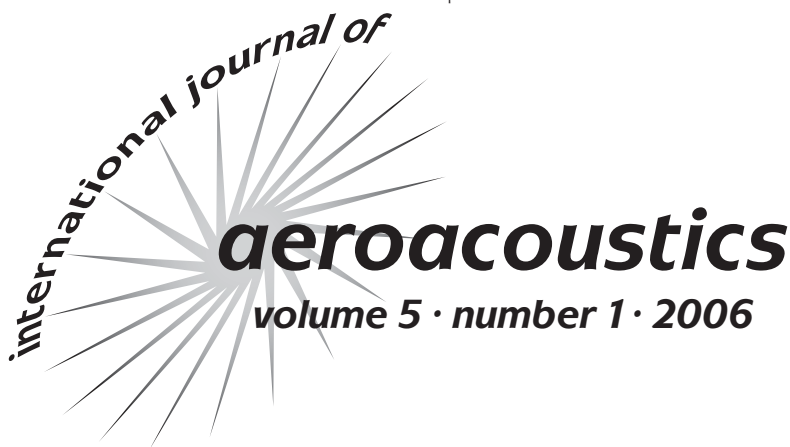


Rotor wake vortex definition-evaluation of 3-C PIV results of the HART-II study

by

**Casey L. Burley, Thomas F. Brooks, Kristen Y. Rozier,
Berend van der Wall, Hughes Richard, Markus Raffel,
Philippe Beaumier, Yves Delrieux, Joon W. Lim, Yung H. Yu,
Chee Tung, Kurt Pengel and Edzard Mercker**

reprinted from



published by MULTI-SCIENCE PUBLISHING CO. LTD.,

5 Wates Way, Brentwood, Essex, CM15 9TB UK

E-MAIL: mscience@globalnet.co.uk

WEBSITE: www.multi-science.co.uk

Rotor wake vortex definition-evaluation of 3-C PIV results of the HART-II study

Casey L. Burley, Thomas F. Brooks, Kristen Y. Rozier

NASA Langley Research Center, USA

Berend van der Wall

DLR, Braunschweig, Germany

Hughes Richard and Markus Raffel

DLR, Gottingen, Germany

Philippe Beaumier and Yves Delrieux

ONERA, France

Joon W. Lim, Yung H. Yu, and Chee Tung

US Army AFDD, NASA Ames Research Center, USA

Kurt Pengel and Edzard Mercker

DNW, Netherlands

ABSTRACT

An evaluation is made of extensive three-component (3-C) particle image velocimetry (PIV) measurements within the wake across a rotor disk plane. The model is a 40 percent scale BO-105 helicopter main rotor in forward flight simulation. This study is part of the HART II test program conducted in the German-Dutch Wind Tunnel (DNW). Included are wake vortex field measurements over the advancing and retreating sides of the rotor operating at a typical descent landing condition important for impulsive blade-vortex interaction (BVI) noise. Also included are advancing side results for rotor angle variations from climb to steep descent. Using detailed PIV vector maps of the vortex fields, methods of extracting key vortex parameters are examined and a new method was developed and evaluated. An objective processing method, involving a center-of-vorticity criterion and a vorticity “disk” integration, was used to determine vortex core size, strength, core velocity distribution characteristics, and unsteadiness. These parameters are mapped over the rotor disk and offer unique physical insight for these parameters of importance for rotor noise and vibration prediction.

SYMBOLS

C rotor blade chord, 0.121 m
 C_T rotor thrust coefficient, thrust/ $\rho\pi R^2(\Omega R)^2$

CV	center of vorticity in (x,y) plane, m
DNW	German-Dutch Wind tunnel
DLR	German Aerospace Center
HART	HHC Aeroacoustic Rotor Test
HHC	Higher Harmonic Control
k	grid point indices
j	indices for instantaneous image
LDV	Laser Doppler Velocimetry
LLS	Laser Light Sheet
n	number associated with analytical velocity profile, Eq. 5
R	rotor radius, 2 m
r_C	vortex core radius, m
r'_C	core radius associated with Rankine vortex, m
r'_C/r_C	shape factor for vortex velocity profile
u,v,w	velocity components for x,y,z coordinates, m/s
V_T	rotor hover tip speed, $R\Omega$ (218 m/s)
v_C	'spin' velocity at r_C , m/s
$(x,y,z)_{TUN}$	windtunnel coordinate system: (x_{TUN} positive downstream, y_{TUN} positive starboard, z_{TUN} positive up).
x,y,z	PIV image frame coordinates, m, Fig. 4.
α	rotor shaft angle with respect to z_{TUN} axis, deg
δ	vortex wander parameter, m
Γ_C	circulation within r_C , m/s^2
σ	standard deviation of parameters derived from instantaneous images
Ω	rotor rotation frequency, rad/s
ω_z	vorticity normal to (x, y) plane, s^{-1}
Ψ	blade azimuth angle (0^0 aft), deg.

INTRODUCTION

Helicopter rotor noise has been measured and studied intensely over that last several decades in order to understand and predict the noise generation as well as determine methods for control and reduction. In particular, rotor blade vortex interaction noise (BVI) has received much of the attention due to its significance during descent. When BVI noise occurs, it can dominate the radiated noise field and adversely affect community acceptance of rotorcraft (Refs. 1-4). In addition to BVI noise, rotor broadband noise has also been shown to be significant and even dominate the radiated noise field for certain operating conditions, such as shallow climb (Refs. 5, 6). The rotor broadband noise sources are namely due to blade wake interactions (BWI noise), which is the interaction between a blade and the turbulent wakes of preceding blades, and the interaction between the airfoil blade and the turbulence produced in its own boundary layer and near wake (self noise). Both BVI and BWI noise sources result from the blade interacting with the rotor wake and its associated turbulent field. In addition to

increasing noise, interaction of the wake with the rotor also adversely affects vibration levels.

Significant advances in understanding and prediction of these noise sources were made in part due to the benchmark database made available through the HART I test program of 1994 (Refs. 7-9). High spatial and temporal resolution acoustics, unsteady blade pressures, and blade dynamics measurements were obtained for a 40% scale model Bo105 main rotor. In addition wake measurements using LDV and LLS were obtained only at limited locations (Refs. 10, 11). The main objectives were to develop and improve the physical understanding and prediction capabilities of blade vortex interaction noise with and without higher harmonic pitch control (HHC). Significant advances in aeroacoustic analysis and their validations were achieved, substantially due to improved free-wake and prescribed wake models (Refs. 12-17). It was determined that HHC reduced noise and vibration by increasing blade-vortex-miss-distance and altering the wake geometry and strength (Refs. 9, 14, 18, 19). More detailed wake measurements were found to be needed in order to fully understand the effects of HHC and to validate the prediction models.

In the last decade, advances in measurement techniques and digital cameras have allowed measurements of the rotor wake to be more easily attainable. Measurement systems such as 3-D LDV, and PIV (Particle Image Velocimetry), are now routinely used to acquire instantaneous velocity measurements over relatively large areas and volumes. Leishman (Refs. 20, 21), Han (Ref. 22), Coyne (Ref. 23), Bhagwat (Refs. 24, 25), and Martin (Ref. 26) have measured the tip vortex generated by a one- and two-bladed rotor in hover using 3-D LDV. The swirl and axial velocity profiles of the tip vortex as it ages as well as derived parameters such as core size, strength, and turbulence quantities have been documented in detail. Martin (Ref. 27) also examined and compared the wake (up to one rotor revolution) of a single bladed hovering rotor with 4 different tip shapes. The initial vortex structure and strength was shown to vary significantly as a function of tip shape. Heineck (Ref. 28) used 3-C PIV to examine the wake of 2-bladed rotor in hover for wake ages up to 270 degrees. The effect of vortex wander and the effect it may have on determining core size from the measured data was presented. McAlister (Ref. 29) also used 3-C PIV to examine the wake of a hovering rotor. The effect of a turbulence-generating device attached to the tip of the blade was shown to significantly alter the size and strength of the tip vortex.

PIV measurements have also been made for rotors in forward flight. Raffel (Ref. 30) compared 3-D LDV with 2-C PIV measurements taken at one rotor azimuth location. The advantages and differences of the measurement techniques for application to measuring rotor vortex properties were discussed. More extensive 2-C wake measurements have been obtained on the advancing side of a large model rotor for a number of streamwise locations (Ref. 31). Similar measurements were also obtained for a prop rotor (Ref. 32). In that test, multiple vortices with opposite sense in rotation were found.

In 2001, a major international cooperative research program Higher-harmonic-control Aeroacoustics Rotor Test II, called HART II (Ref. 33-36) was conducted under US/German and US/French Memoranda of Understanding, by researchers from

the German DLR, the French ONERA, the Netherlands DNW, NASA Langley, and the US Army Aeroflightdynamics Directorate (AFDD). HART II is a comprehensive experimental program conducted with a 40% Mach scaled model of a BO-105 main rotor in the Duits-Nederlandse Windtunnel (DNW) in the Netherlands. The objective of the test was to obtain extensive 3-C PIV measurements of the rotor wake over both the advancing and retreating sides of the rotor disk, along with acoustic directivity measurements, unsteady blade surface pressure measurements, and blade deformation measurements in order to (1) to investigate the physics of BVI, broadband noise and vibration reduction concepts with the HHC technology, (2) to develop an analytical prediction capability for rotor BVI and broadband noise, and (3) to generate a comprehensive experimental database for code validation.

In this paper, an analysis of the HART II 3-C (3-component) PIV wake measurements are made in order to determine for non-HHC rotor conditions, wake vortex definitions for a range of rotor angles from climb to descent. PIV vector maps were obtained over the advancing and retreating side of the rotor. Details of the vortices, such as core size, strength, core velocity characteristics, and unsteadiness are quantified and determined as a function of rotor angle and nominal wake age. Determination of these quantities from the measurements using different methods are performed and assessed. An objective processing method is developed and utilized to determine vortex definition.

ROTOR MODEL TEST DESCRIPTION

The HART II program was conducted in the open-jet, anechoic test section of the Large Low-speed Facility (LLF) of the DNW, which has an exit nozzle of 8 m by 6 m that provides a 19m-long free jet with a low-turbulence potential core.

The set-up for the PIV measurement portion of the test is shown in Fig. 1. The rotor hub was located nominally 7 m downstream from the nozzle exit and maintained at 0.92 m above the tunnel centerline. The rotor is a 40-percent, dynamically and Mach-scaled Bo105 main rotor with a diameter of 4 m. It consists of four hingeless blades that have a pre-cone of 2.5 degrees at the hub. The rectangular planform blades have a chord length of 0.121 m, NACA 23012 sections (with tabbed trailing edge), -8 degrees linear twist and standard rectangular tips. For the HART II test, the rotor was operated at a nominal rpm = 1041 (hover tip speed of 218 m/s), $C_T = .0044$, and an advance ratio of 0.15, for 6 rotor shaft angles, $\alpha = -6.9^\circ$ (climb), -3.6° , -0.5° , 2.4° , 5.3° , and 11.5° (steep descent). The baseline condition at rotor shaft angle of 5.3° , was run for selected HHC conditions. More detailed information on the rotor characteristics are given in Ref. 36. For this paper, only the non-HHC conditions are considered.

Three-Component PIV Measurements

The rotor wake was measured on both the advancing and retreating sides of the rotor using 3-C PIV. The measurement locations (cut planes) are shown in Fig. 2. The two rotor azimuthal orientations, (a) and (b), are used in order to keep the blades from interfering with the wake measurements. There were approximately 50 locations on each of the advancing and retreating side for the baseline and 2 HHC conditions. For limited locations on the advancing side (labeled with red numbers) PIV measurements

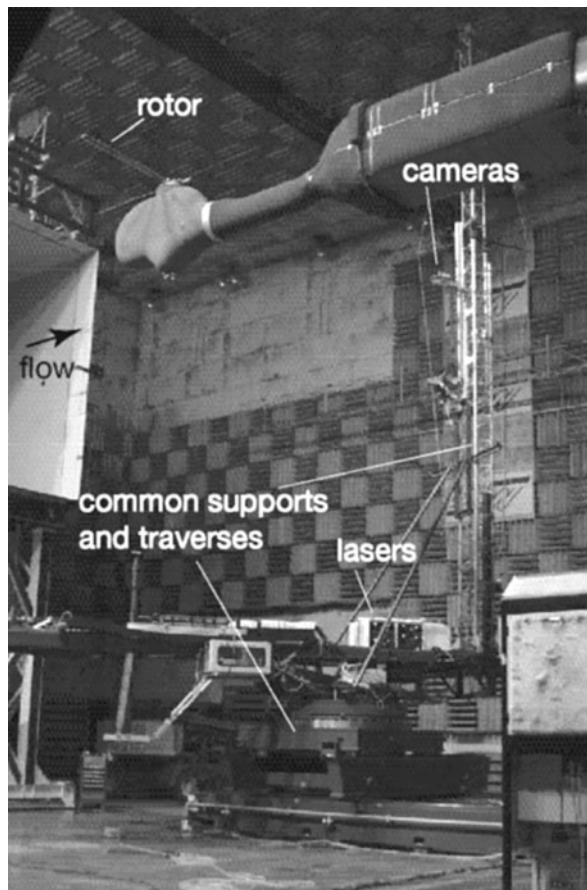


Figure 1. HART II rotor and 3-D PIV setup in the DNW test section.

were made for the 6 shaft angles. At every PIV measurement location, at least 100 instantaneous vector map images were obtained. The nominal wake age associated with each of the PIV measurements were determined and are provided in Table 1 of the Appendix.

The PIV setup implemented for this test consisted of five digital cameras and three double pulse Nd:YAG lasers. The lasers and cameras were mounted onto a common traversing system in order to keep the distance between the cameras and the light sheet constant while moving to different measurement locations within the rotor wake. Figure 1 shows the rotor and traverse equipment in the DNW test section. The 5 cameras were located on the 15 m vertical tower and the lasers were located underneath the rotor. Four of the cameras were for the 3-C PIV measurements. The fifth camera was used to visually check seeding prior to PIV data acquisition. To obtain measurements on the

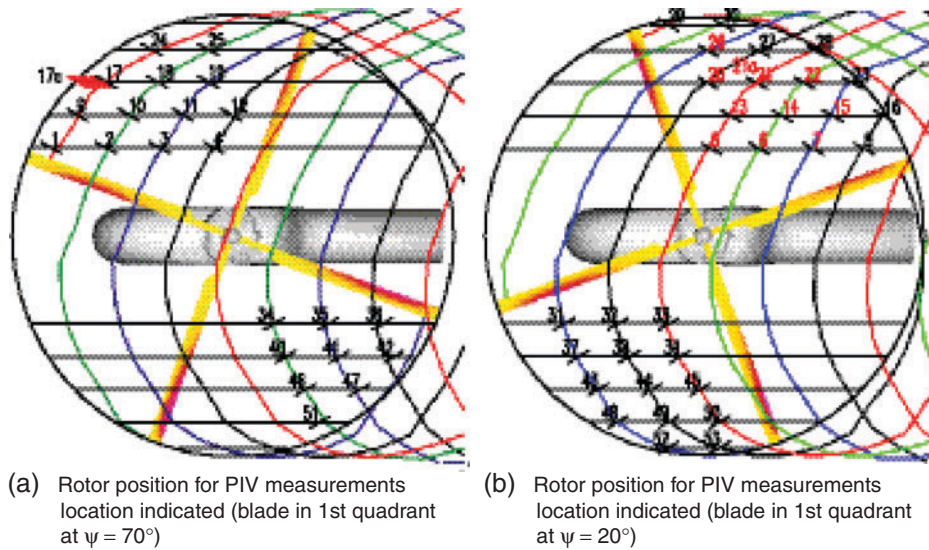


Figure 2. Schematic showing the (cut plane) locations of the 3-C PIV rotor wake measurements.

retreating side the entire support structure and tower was repositioned to the retreating side. Measurements could be continued without recalibration. Further details of the PIV systems see Ref. 34.

At each of the cut planes shown in Fig. 2, 3-C PIV measurements were obtained simultaneously from two systems. This was done in order to obtain both a large image frame of the vortex and its surrounding flow as well as a small, higher resolution, image frame focused primarily on the vortex core region. Figure 3 presents an example result from each system (to be subsequently discussed). Each camera had a resolution of 1024 by 1280 pixels and was digitized to 12 bit. The cameras were separated vertically on the tower by 5.2 m, with one camera from each system above and below the rotor plane. For the higher spatial resolution system, 300 mm lens were used and for the lower resolution, larger image frame system, 100 mm lens were used.

Three double pulsed Nd:YAG laser systems (each 2×320 mJ) were located on the base of the common support system as shown in Fig. 2. A large (nominally 1.5 m) light sheet of nominally 7 mm thick was oriented 30.6° with respect to the wind tunnel x_{TUN} axis. The black cut lines shown in Fig. 2, indicate the top view of the light sheet orientation. The horizontal distance between the light sheet and cameras was 5.6 m. The cameras and lasers were synchronized with the one-per-rev signal given by the rotor, which allowed for recording at desired phase-angles of the rotor blade.

Flow seeding was accomplished by a specially designed seeding rake located in the settling chamber, immediately upstream of the turbulence screen. The rake was nominally $3 \text{ m} \times 4 \text{ m}$ and was connected to Laskin nozzle particle generators. Di-2-Ethylhexyl-Sebacat (DEHS) was used as the seed material. The mean diameter of the

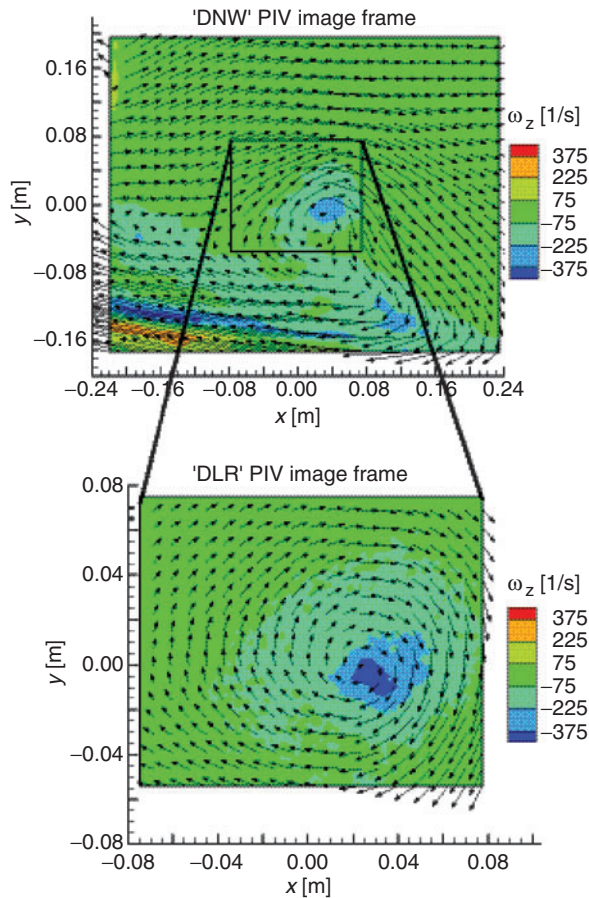


Figure 3. DNW and DLR PIV measurement image frame areas. Every 3rd vector shown in DNW image, every 5th vector shown in DLR image.

particles generated was below 1 μm . The seeding rake was remotely moved both vertically and horizontally during testing to seed the area of interest.

The procedure was designed to measure the wake from the same blade at all cut line locations indicated in Fig. 2. This would allow for the tip vortex to be investigated in detail from its creation through its evolution as it convected and traversed downstream throughout the rotor disk region. Because of this, any questions of blade-to-blade differences could be avoided. (Blade to blade differences were, however, examined in this test, but results are not reported here.)

The measurement process commenced at one of the most upstream locations indicated in Fig. 2 and progressed downstream along a line of constant y_{TUN} (indicated as the black horizontal lines). For example, the starting locations for locations shown in

Fig. 2 (a) are cut lines #1, #9, #17, and #24. The reference rotor position is identified as $\psi = 70^{\circ}$, which is the (nominal) azimuth position of the blade located in the first rotor quadrant. The actual measured blade azimuths are at $\Delta\psi = 3.5^{\circ}$ later blade position due to a time lag introduced inadvertently during testing. The blade azimuths in this paper are given at nominal values. The camera and lasers are synchronized with the one-per-rev signal of the rotor and hence PIV image data is acquired when the appropriate blade is positioned in the reference location. Image pair sampling was triggered every 3rd rotor revolution, if the rotor maintained a constant rpm, otherwise the trigger could be slightly longer (Ref. 34). Once 100 image pairs were obtained the common support system was traversed downstream to the next cut line. The rotor reference blade angle was then incremented by 90° in order to continue measuring the wake from the same blade. The procedure was repeated in a similar manner for all locations shown in Figs. 2 (a) and 2 (b).

PIV Image Processing

Figure 3 presents example DNW and DLR results for the measurement cut plane location of #21 ($x_{\text{TUN}} = 0.725$ m, $y_{\text{TUN}} = 1.4$ m) (see Fig. 2 (b)). The DNW obtained PIV measurements over a large area that was nominally 45.3 cm by 36.7 cm, which is approximately 4 blade chords by 3 blade chords. The PIV images were processed with a 32×32 interrogation window size that resulted in a resolution of 0.0058 m/vector. The DLR PIV measurement area was smaller (nominally 15.2 cm by 12.9 cm, which is approximately 1.2 blade chords by 1 blade chord) and was centered within the larger DNW area on the vortex core region. The DLR PIV image shown in Fig. 3 was processed with interrogation window sizes of 24×24 pixels, which results in a resolution of 0.00154 m/vector, nearly 4 times that of the DNW data. For the 24×24 pixel interrogation window, the maximum vorticity was found to be about 16% higher than that obtained using data processed with the 32×32 window. Velocity vector fields were obtained from each PIV image-pair using the cross-correlation method (Refs. 34, 37, 38). In Fig. 3 and in presentations to follow, the magnitude of velocity vectors for the DNW frames, 14.2 m/s equates to a “scale length” of 10 cm, and for the DLR frames, 33.3 m/s equates to 10 cm.

PIV data validation

PIV velocity vector fields can contain incorrect vectors (outliers). Before using the PIV data it is important to identify and replace the outliers with valid data to insure the accuracy of subsequent results. Sources of outliers in the HART II data included seeding problems, low laser light intensity, blade in the field of view (causing reflection and obstruction), and large laser pulse separation times (Refs. 34). Prior to constructing the final 3-C vector fields a scan of the vectors in each of the 2-C vector fields are checked. Each vector is compared with each of its eight neighbors. If the difference in magnitude exceeds a specified threshold, its tag is increased by one. If a vectors tag value is greater than 5 is removed and replaced using a bi-linear interpolation from the surrounding valid neighbors. The threshold used was always slightly conservative in order to ensure that no good vectors were removed. For the DNW data set outliers were

found to be minimal and when they did occur were found to be mainly concentrated near the edges of the images where laser light intensity was lowest. For the DLR data set the outliers were even less than for the DNW data set.

Vortex Alignment

For this study, the PIV plane cut 30.7° orientation is used for nominal alignment to the normal to the vortex axis. Based on pretest wake predictions, tilt angles of the vortex with respect to the cut lines along $y_{TUN} = 1.94, 1.7, 1.4, 1.1, 0.8, -0.8, -1.1, -1.4, -1.7,$ and -1.94 m would be expected to be on the order of $\theta = 35^\circ, 30^\circ, 20^\circ, 0^\circ, -3^\circ, 20^\circ, 10^\circ, -3^\circ, -20^\circ,$ and -35° . Because of tip vortex roll-up, there is some variation from this along the y_{TUN} cut lines. In addition, general wake unsteadiness can cause instantaneous PIV image frame orientation differences.

It is beyond the scope of this paper to determine tilt and account for it in the derivation of vortex parameters. A rough estimate is that local velocities and dimensions can be in error on the order of $\pm(1-\text{Cos}(\theta))$ or about $\pm 15\%$ for $\theta = \pm 30^\circ$. This is further discussed in the text, but the methods used to determine key vortex parameters are expected to result in error of less than half of this.

WAKE PRESENTATION

A series of 3C PIV results are presented to show the basic character of the rotor wake, as well as to successively show derived parametric presentations of the wake.

Figure 4 illustrates the view orientation of the PIV cut planes (of Fig. 2 and Table 1), presented in the next figures. The view, as well as each cut plane is orientated 30.7° from the tunnel axis. The DLR and DNW image frames, which coincide with the cut planes, are defined with coordinates (x, y) , where y is aligned with the z_{TUN} axis. The frames are in rows such that the y axis cuts through the same y_{TUN} axis value. The (x, y) planes are positioned progressively lower (more negative z_{TUN}) for increasing x_{TUN} . This is because the camera positions were lowered for the more downstream locations, in order to capture the vortices. The x axis is offset in angle (30.7°) from the downstream (x_{TUN} axis) direction. For the advancing side cuts, the PIV cameras were on the positive y_{TUN} side, out of the flow, so the originally processed images were

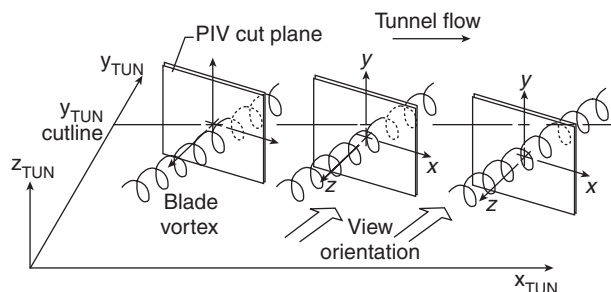


Figure 4. Sketch to illustrate the view orientation of PIV cut planes presented in figures to follow. Advancing side cuts are shown.

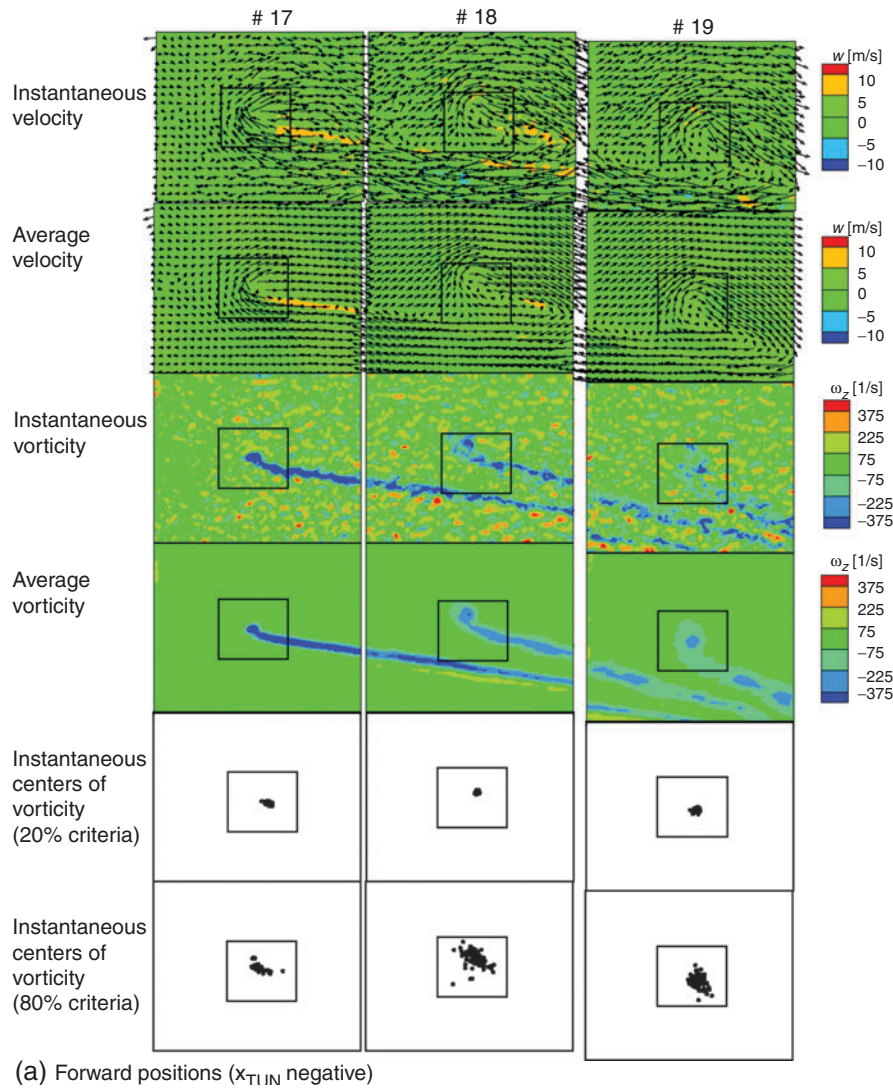


Figure 5. Advancing side, Rotor angle $\alpha = 5.3^\circ$ (baseline condition) – velocity and derived parameter maps. PIV image frames positioned along $y_{TUN} = 1.4$ m.

reversed for this presentation. For the retreating side, the cameras were on the negative y_{TUN} side, so no image reversal was necessary.

Wake Images for Baseline Rotor Condition

Advancing Side

For a rotor baseline descent condition important for BVI noise, Fig. 5 shows wake images for six PIV cut planes along $y_{TUN} = 1.4$ m, viewed in the manner described for

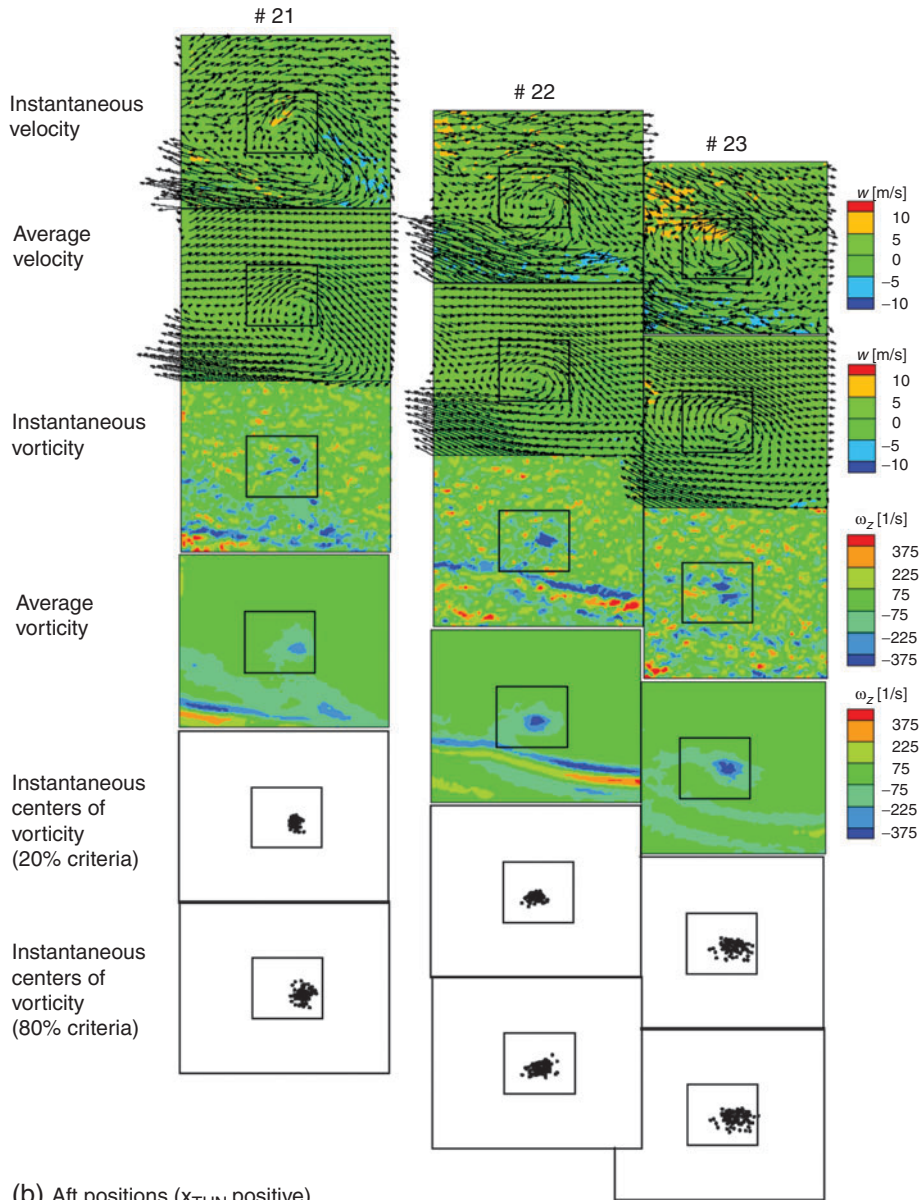


Figure 5, cont'd.

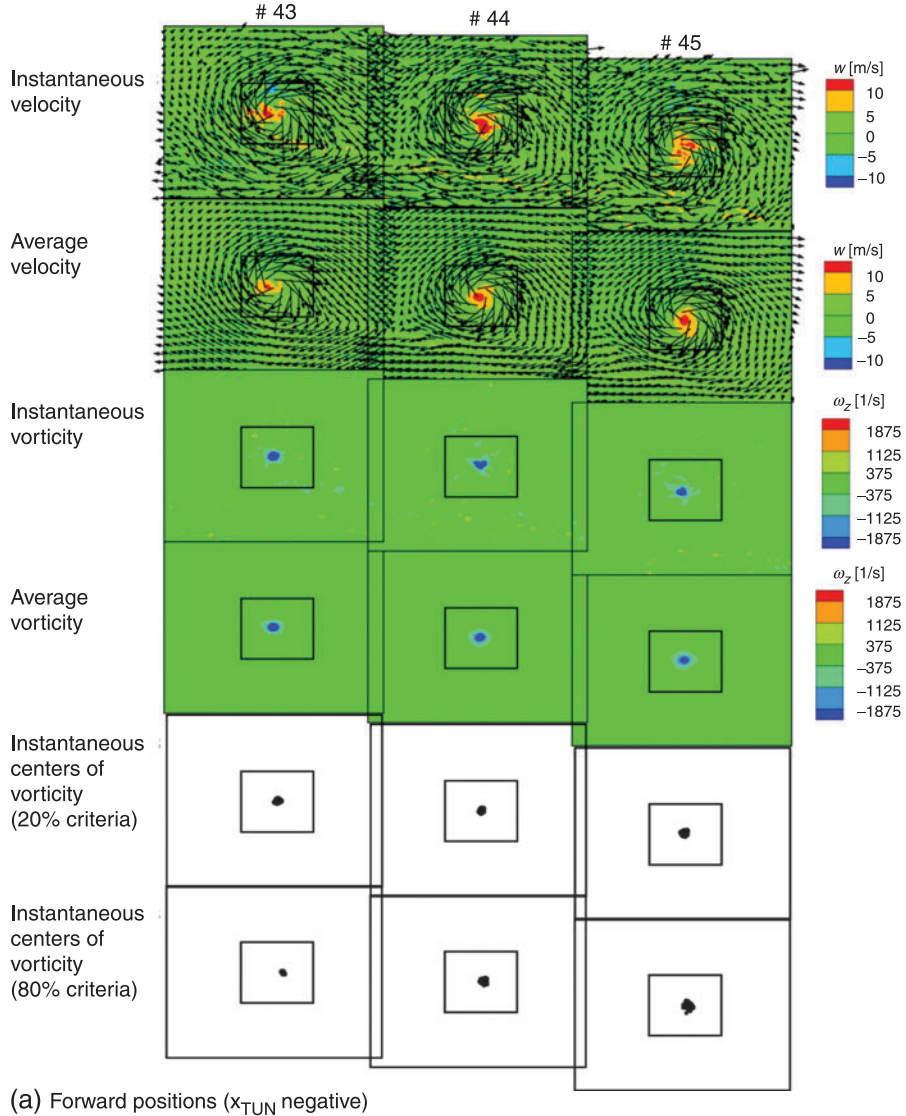


Figure 6. Retreating side, Rotor angle $\alpha = 5.3^\circ$ (baseline condition) – velocity and derived parameter maps. PIV image frames positioned along $y_{TUN} = -1.4m$.

Fig. 4. For comparison, Fig. 6 shows similar wake images for the retreating side. Corresponding to Fig. 2 (and Table 1), the cut planes are #17, 18, 19, 21, 22, and 23. Because the spacing between frames corresponds to $\Delta x_{TUN} \cos 30.7^\circ$ in this view, frames overlap in some regions. Where this happens, the frames at larger x_{TUN} are partially covered. The velocity and vorticity data shown in all frames are from PIV

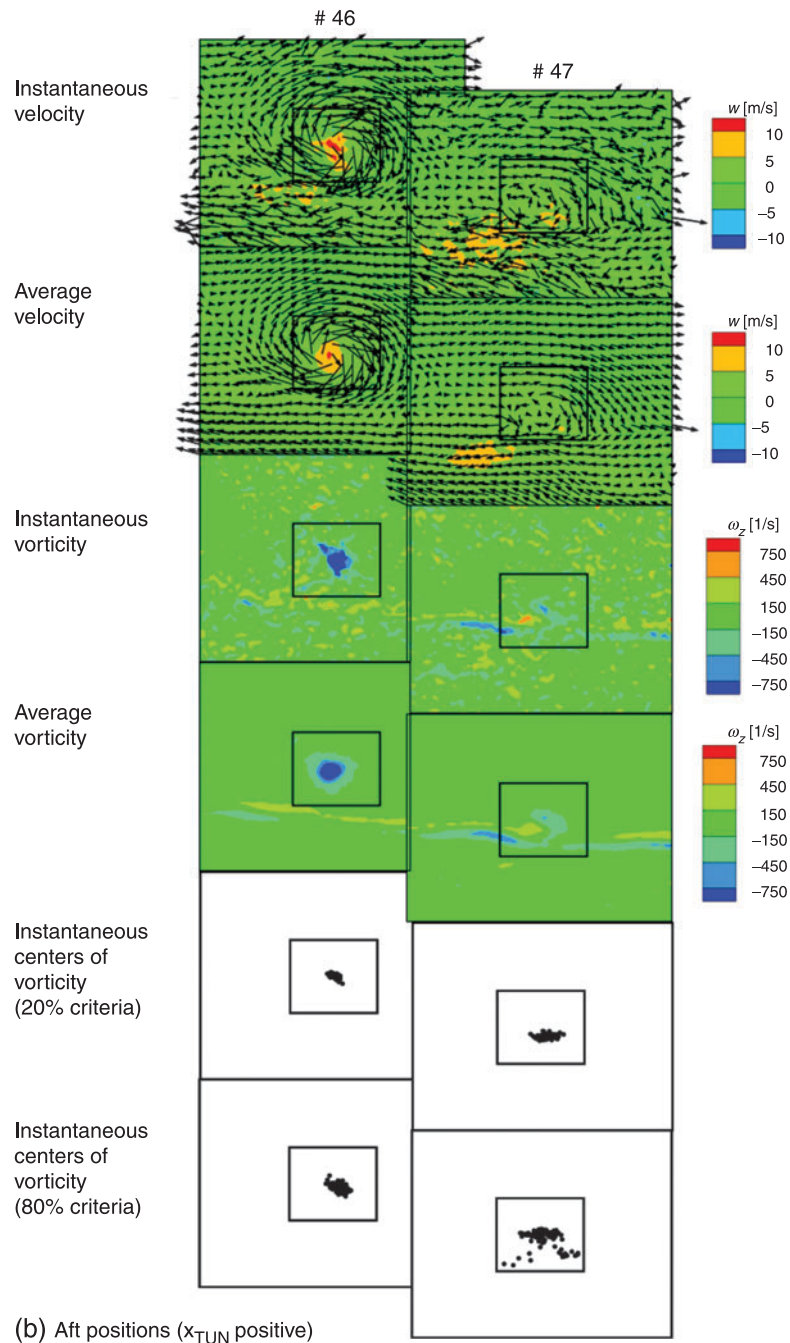


Figure 6, cont'd.

images and processing by DNW. The outline of the smaller DLR frame is shown within each. It contains the primary vortex and is used in subsequent determination of detailed vortex parameters. Because of its finer spatial resolution, DLR data were used to generate all the instantaneous centers of vorticity (subsequently defined).

The top frames of Fig. 5 present processed velocity vector maps for instantaneous points in time for the wake regions captured. Each arrow represent the x and y components of velocity, after a mean velocity is removed to permit a (much) better viewing of the vortex field. That is, $\vec{U}(x, y, z = 0) = u\hat{i} + v\hat{j} + w\hat{k}$, which is also written as, $\vec{U} = \vec{U}_{Tot} - \vec{U}_0$, where $\vec{U}_0 = u_0\hat{i} + v_0\hat{j} + w_0\hat{k}$ is the mean velocity within the region of the larger frame but outside of the smaller frame. These \vec{U}_0 values are listed, in Table 1 of the Appendix, for the frames shown. (It is noted that in previous LDV flow study⁸ presentations for this rotor, a set estimated value of the equivalent of \vec{U}_0 were used for all locations over the rotor disk. But here by this method, one sees that there is a substantial variation across the rotor disk region – with stronger downwash components in the downstream direction.) As previously mentioned for the DNW frame presentations, the velocity vector magnitudes can be equated to the frame size (width is 45.3 cm with 14.2 m/s equating to about 10 cm). The magnitude of the w velocity component is indicated by color contour under the (u, v) vectors. Negative w values indicate component is directed into the page. For clarity, only every third vector along a line is plotted, so only 1/9th of the vectors are plotted.

The second row of frames from the top of Fig. 5 contain averaged velocity vectors determined by simply summing the 100 instantaneous vector maps and dividing by 100. Because of unsteadiness (or wander) in vortex position and flow details between the instantaneous vector fields, smearing of detail occurs, but the basic mean wake-shear-flow character is better revealed.

The next two series of frames are of instantaneous and averaged vorticity distributions generated by the corresponding velocity distributions above, that is $\omega_z = (\Delta u / \Delta y - \Delta v / \Delta x) / 2$. Here Δx and Δy correspond to the DNW grid spacing. By the right-hand-rule, negative ω_z indicate rotation is clockwise in this view. The vorticity distribution presentations, unlike the velocity presentations, are independent of the choice of any mean velocity values. They are seen to reveal, more clearly, the early wake vortex sheets in the upstream direction (frames on the left), the roll-up evolution, and separation of the blade vortices in the downstream direction. For example, one can see signs of a near, but not direct, blade vortex interaction (BVI) on image frame #22. The lines of counter rotating shear from a blade's two boundary layers identifies the wake of a recent blade passage. This shear-line pair has little net circulation and represents the "2D" mid-blade wake that eventually dissipates and does not roll-up. (A PIV cut plane, if placed nearly normal to these present cut planes, would reveal the same wake to have net circulation shear lines and thus have a tendency to roll-up in that plane (much like the view of frame #17). The present data, of course, only resolves the PIV cut-plane normal component of vorticity.)

In the bottom two frames of Fig. 5, the centers of vorticity, CV , of each of the 100 images (that meet criteria listed) are presented. The CV positions are used to identify the vortex center in each frame for vortex parameter calculations. The scatter of these CV positions can also be viewed as representing the degree of wander (non-repeatability) in the instantaneous images. The center of vorticity is defined as

$$CV = \frac{\sum_k (\omega_z)_k \cdot (x_k, y_k)}{\sum_k (\omega_z)_k} \quad (1)$$

where k are grid point indices taken over the whole DLR frame. For most cut planes, not all 100 instantaneous images have CV positions determined. Excluded are images where the maximum values of ω_z do not exceed a 20 % threshold of the maximum ω_z , found by considering all 100 image frames. This eliminates extraneous images where seeding, laser light, other PIV conditions, or an occasional vortex-formation disruption produced ill-defined vortices. In frame #19 of Fig. 5, for example, 11 of the 100 images are not included. However, most frames only excluded 5 or less. An additional criterion is used to properly locate the vortex within each frame. In the evaluation of Eq. (1), only those values of ω_z that are of a correct sense (as determined by evaluation of Eq. (1) for an averaged vorticity distribution) and that exceed a certain percent of the maximum value of ω_z within each image are included. In Fig. 5, the results of applying 20% and 80% criteria are shown. The use of 20% eliminates “noise” within the frame, while capturing the vortex and its shear layer. Applying an 80% criterion is found to substantially isolate the vortex itself, even when attached to a strong shear sheet – such as that seen in frame #17 for the young vortex. Because of vortex wander the 80% criterion is seen to produce much larger scatter of CV . For some cut plane locations, especially where strong shear is present and localized “hot spots” occur on instantaneous frames, the criteria (especially 80%) can create false CV locations in some cases. Although this has not been fully evaluated, this is more of a problem when the vortex itself is very weak or highly fragmented, as would be case for vortices after direct BVI.

Figure 5 gives some illustration of vortex axis tilt with respect to the cut plane. Considering frame #22, there is not a pronounced w velocity component acting through its center, although an asymmetry is noted in w across this clockwise-rotating vortex in the image frame y direction. This indicates that the axis of the vortex (if modeled as a rotating tube with axis along the center of the tube) is somewhat tilted with respect to the cut plane – roughly in the negative x direction from the positive z axis (see Fig. 4). Other evidence of this tilt is seen in the slight vortex core elongation, in contrast to a purely circular pattern – particularly seen in the vorticity plots. This elongation is also seen in the distribution of CV .

Retreating Side

Figure 6 has the same presentation as Fig. 5 (except for amplitude scaling of vorticity, to be discussed) for $y_{TUN} = -1.4$ m on the retreating side. The five frames shown are numbers #43-47, as identified in Fig. 2. As with the rotor advancing side view of

Fig. 4, the observer is on the retreating side and off the rotor, but the view is oriented upstream at 30.7° , rather than downstream. As expected, ω_z is again directed into the page, with corresponding rotation being clockwise. This indicates that the blades that produce these vortices maintain positive lift over their tip region, thereby shedding vortex/vortex sheets of the same orientation as that for $y_{TUN} = 1.4$ m of Fig. 5. A difference in wake character seen for this retreating side is that the vortices are stronger and better defined. The contour color scaling for vorticity amplitude has been extended by a factor of 5 (this can be viewed as a dynamic range change) for frames #43, 44, and 45, in order to properly visualize the vortex core character. (Unfortunately, this tends to wash out flow field details.) For frames #46 and 47, a factor of 2 was used in order not to lose detail in frame #47, but note that this scale somewhat unrealistically elongates the core size appearance in frame #46. Even at an early age (frame #43), the vortex is more fully rolled-up compared to advancing side vortices. This would be expected, due to higher blade tip loading that concentrates the vortex and reduces the extent of the vortex sheet to be rolled-up. The vortex wander is substantially lower and, unlike the advancing side the wander for 80% criterion, is about the same as that of the 20% criterion. The only exception shown is in frame #47 where the vortex is fragmented, likely split due to a blade interaction. Here, the blade boundary layer trail (pair of counter-rotating sheets) is seen to intersect a weakened vortex.

Compared to Fig. 5, a stronger w component is apparent over the vortex core region in Fig. 6. The (u, v) components (shown as vectors) are correspondingly stronger for these retreating side vortices. This w component represents the vortex axial component, to the extent that the PIV cut plane is perpendicular to the vortex axis. A feature similar to Fig. 5 is the asymmetry, across the vortex region, in the sign of w . However, the sign is reversed (top to bottom) indicating, as anticipated, that the vortex is tilted from the cut plane in the opposite direction.

Rotor Shaft Angle Variation - Advancing Side

For the advancing side at $y_{TUN} = 1.4$, the results from PIV cut planes #20, 21, and 22 are presented for different rotor shaft angles. The angles $\alpha = -6.9^\circ$ (climb condition), -3.6° , -0.5° , 2.4° , and 11.5° (steep descent condition) are represented in Figs. 7, 8, 9, 10, and 11, respectively. These use the same presentation as Fig. 5 for $\alpha = 5.3^\circ$.

At the largest negative angle, $\alpha = -6.9^\circ$ (Fig. 7), the vortices and their sheets are below the blade passage region. Here, for the x_{TUN} range shown, the blades do not interact strongly with the vortices. As the rotor angle increases, the vortices and their sheets are seen to approach, convergence, and cross through the region where the blades interact most strongly. At $\alpha = 11.5^\circ$, in Fig. 11, one observes that the blade vortices are well above their vortex sheets. At intermediate angles $\alpha = 2.4^\circ$, -0.5° , and -3.6° (Figs. 8, 9, and 10), one can see the wake of the most recent blade passage - identified, as before, by the lines of counter-rotating shear. In frame #22 for Fig. 10, there appears to be a highly disrupted (burst) vortex from a BVI occurrence - much like that of frame #47 of Fig. 6. In both cases, CV positions are still locatable, although there is question as to the presence of false positions (for the 80 % criterion CV) or even if one should interpret a vortex "per se" as being present.

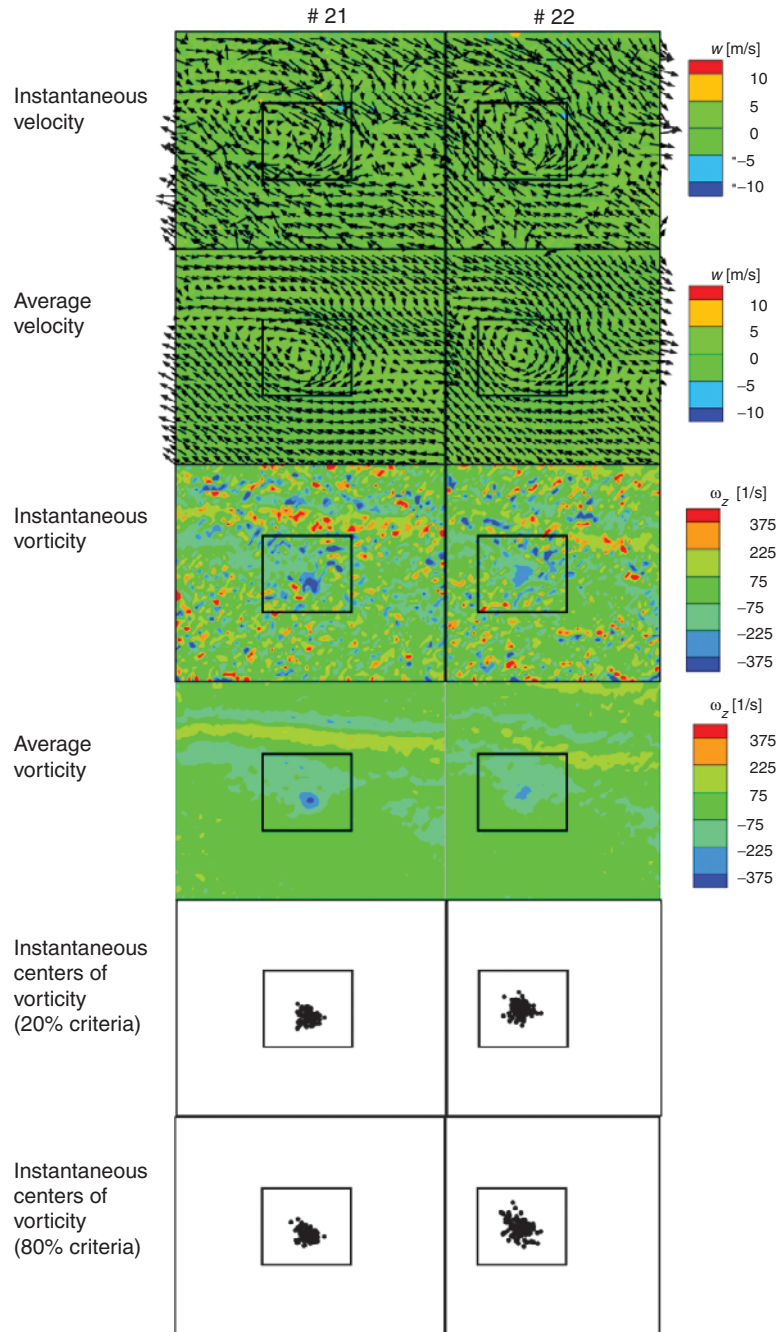


Figure 7. Rotor angle $\alpha = -6.9^\circ$, Advancing side, aft positions (x_{TUN} positive) – velocity and derived parameter maps. PIV image frames positioned along $y_{TUN} = 1.4$ m.

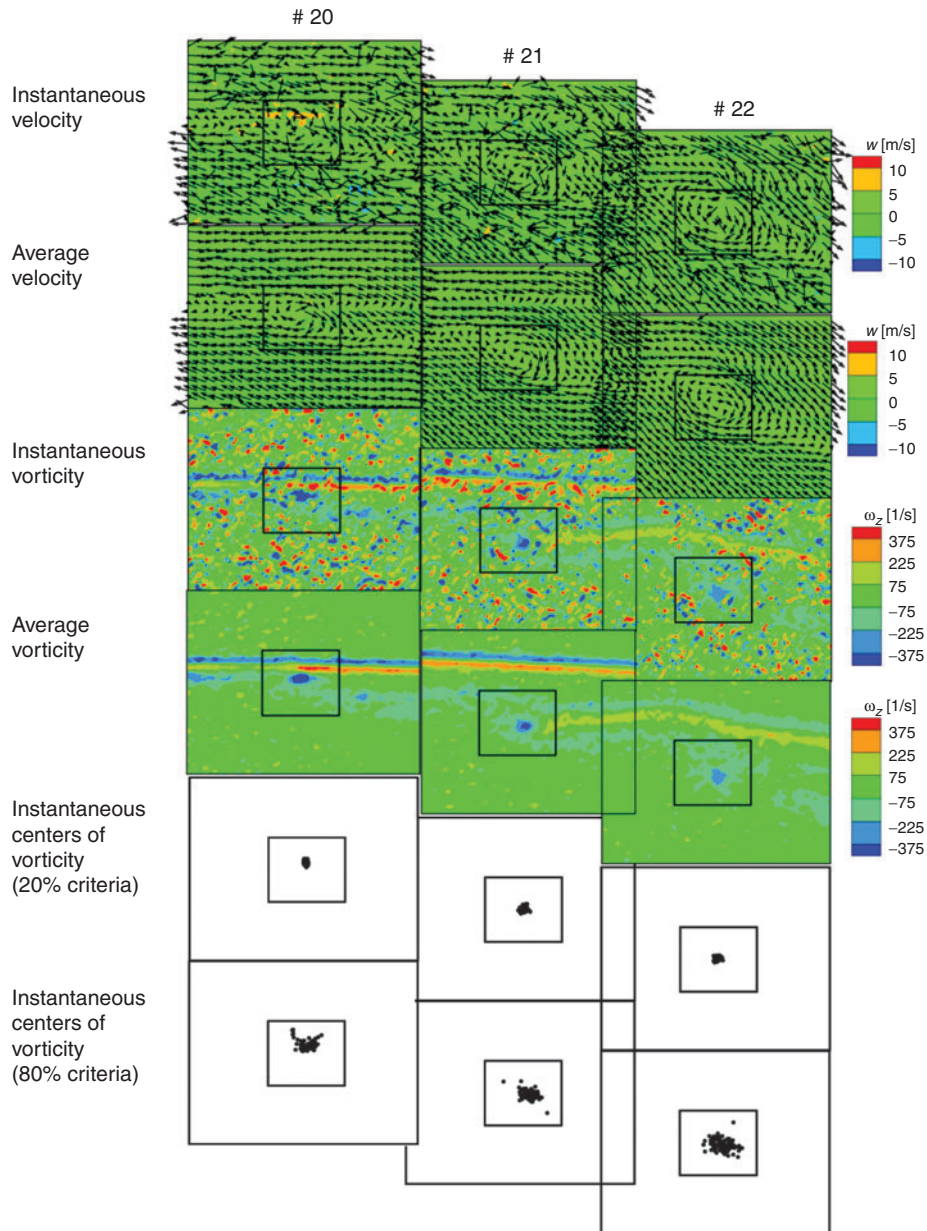


Figure 8. Rotor angle $\alpha = -3.6^\circ$, otherwise same as Fig. 7.

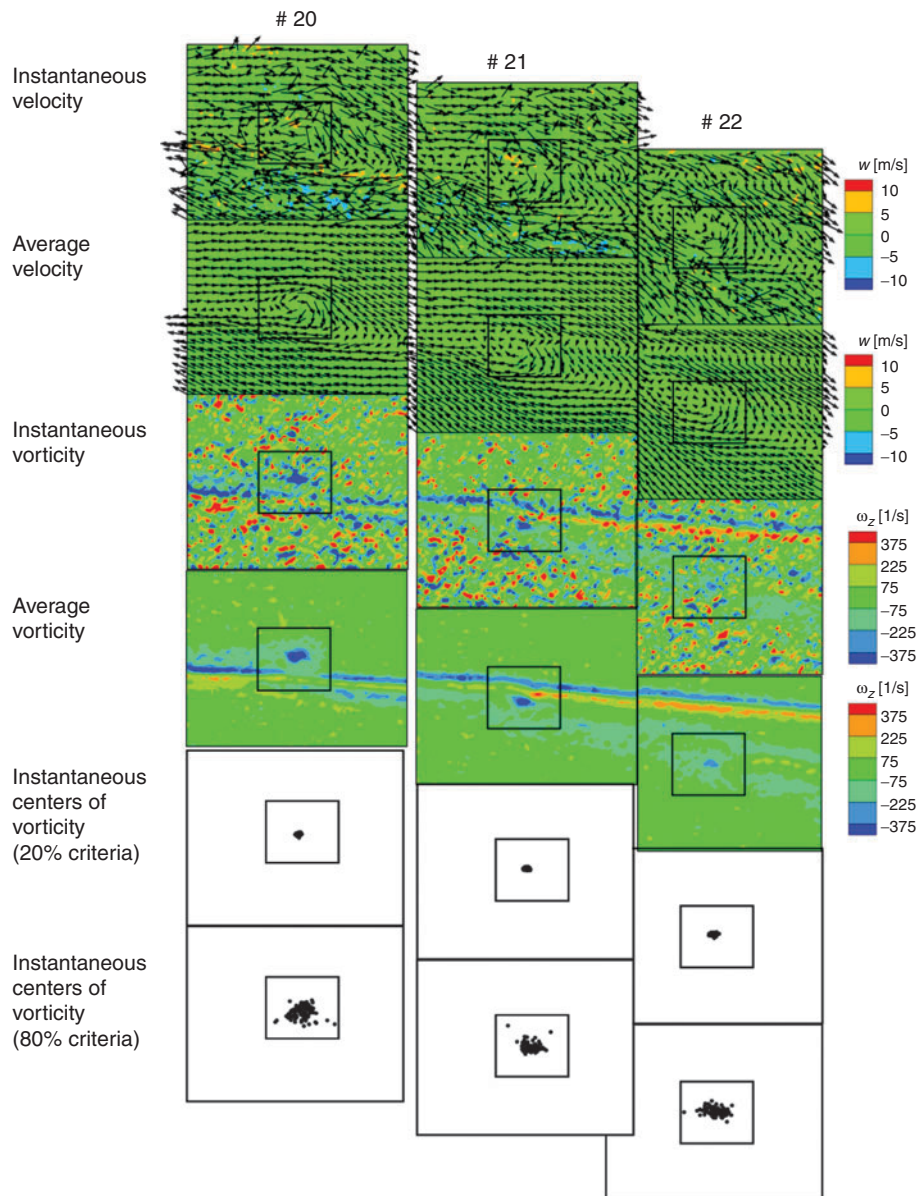


Figure 9. Rotor angle $\alpha = -0.5^\circ$, otherwise same as Fig. 7.

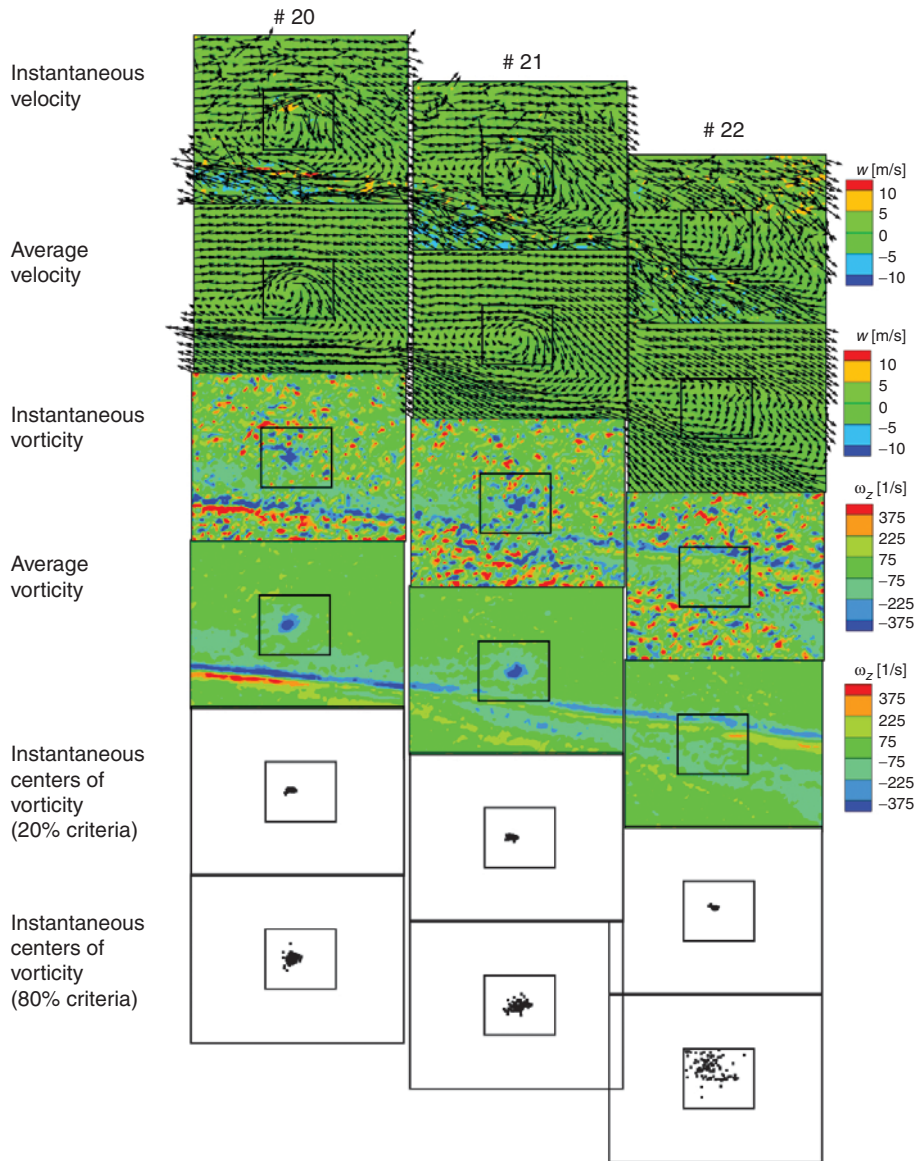


Figure 10. Rotor angle $\alpha = 2.4^\circ$, otherwise same as Fig. 7.

VORTEX DEFINITION AND DISCUSSION

The vortex core size and strength are commonly used for vortex definition. In this section methods to derive these quantities and others are presented in detail. The results are tabulated in Table 1 of the Appendix.

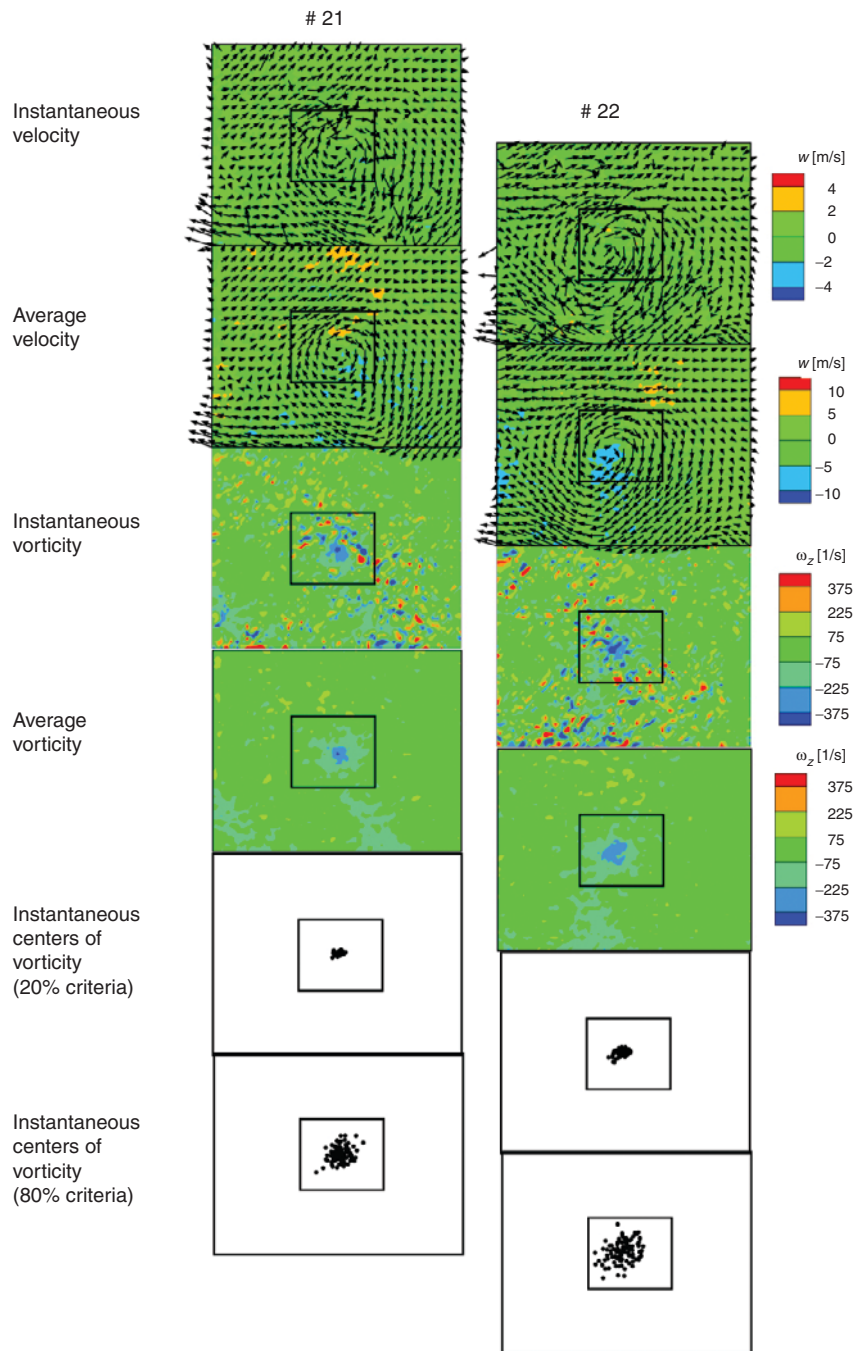


Figure 11. Rotor angle $\alpha = 11.5^\circ$, otherwise same as Fig. 7.

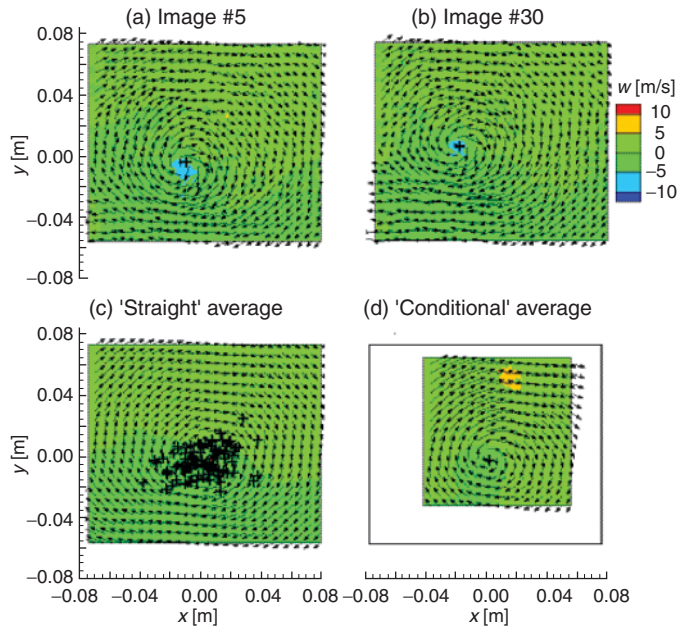


Figure 12. Velocity vector distributions over image frame #22, for $\alpha = 5.3^\circ$ showing instantaneous and averaging methods.

Processing/Calculation Methods

Velocity Cuts

Figure 12 shows four velocity vector distributions corresponding to PIV cut plane #22 for the baseline rotor condition presented in Fig. 5. Different instantaneous velocity vector plots are shown in Figs. 12 (a) and (b) to illustrate a typical degree of variation that occurs between different PIV acquisitions. As done in Fig. 5, Fig. 12 (c) presents the result of straight averaging of all 100 instantaneous fields, which renders a smoothed velocity field presentation. As previously mentioned, this type of averaging can result in smearing of the vortex flow details – because of vortex wandering. In each of the instantaneous plots, Figs. 12 (a) and (b), the respective CV locations (determined using the 80% criteria) are shown. In Fig. 12 (c), all 100 CV locations are shown to indicate the spread or degree of wander as presented in Fig. 5. Figure 12 (d) shows the result of conditional averaging, which is accomplished by first aligning CV locations prior to averaging. This is seen to improve the sharpness of the vortex definition. Note that the image frame is reduced in size due to the removal of non-overlapping regions occurring when the CV locations are shifted.

Figure 13 shows vertical and horizontal velocity cuts taken through the CV for the instantaneous and averaged distributions of Fig. 12. For Fig. 13 (c), an average CV position is used. The horizontal velocity components, plotted along the vertical cut, and the vertical components, plotted along a horizontal cut, give a swirl appearance. Upon defining v_c to equal 1/2 of the difference in peak velocities (identified in figures)

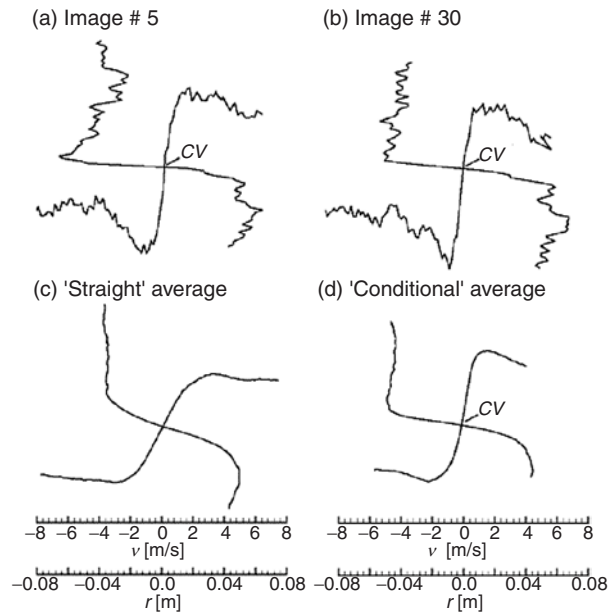


Figure 13. Vertical and horizontal velocity cuts of the respective Fig. 12 distributions.

across the vortex, and r_C to equal 1/2 of the distance between the locations of these peak velocities, the horizontal and vertical cuts give (r_C, v_C) values of (.0139 m, 5.20 m/s) and (.0169 m, 6.54 m/s), respectively, for Fig. 13(a). For Fig. 13(b), these are (.0108, 5.19) and (.0299, 6.05) with units of m and m/s. The ragged character of the instantaneous image cuts give uncertainty to “true accuracy” of the choice of r_C and v_C . The magnitude of v_C is always biased to higher values. Figure 13(c) renders (r_C, v_C) values of (.0299, 3.37) and (.0475, 4.23), which does illustrate that simple averaging produces a larger r_C and smaller v_C compared to instantaneous values. For Fig. 13(d), the values are (.0185, 4.09) and (.023, 4.67), which should be closer to accurate values. But still, the results are still biased because individual vortices of different sizes tend to smear and flatten upon averaging – even if centered.

Vorticity Disk and Analytic Velocity Profile Method.

An alternate method is developed with the intent to determine r_C and v_C that are better based statistically, less bias, and in a form that renders a more complete description of the vortices. Instead of operating on a limited number of velocity cut distributions, vorticity distributions are used. A present limitation to be mentioned is that the procedure intrinsically assumes that the vortex tube is aligned normal to the cut plane. Errors associated with this are subsequently discussed.

Figure 14 shows the vorticity distribution associated with the instantaneous image of Fig. 12(a). The CV position is shown with a radius r defining a circle (or disk) that

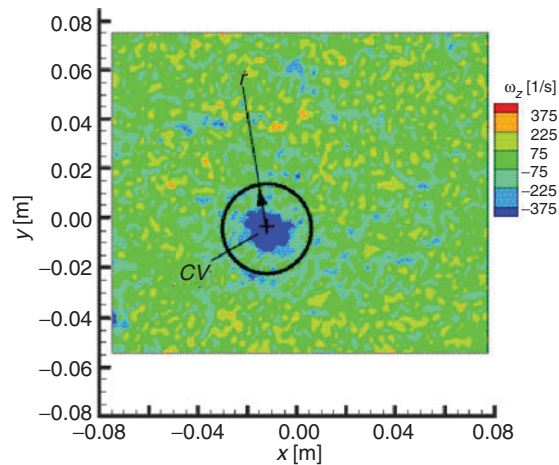


Figure 14. Integration disk with radius r to determine circulation Γ .

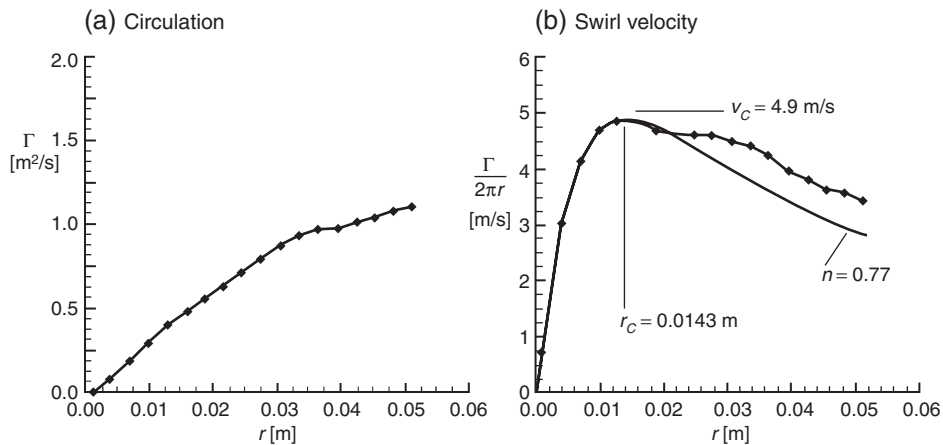


Figure 15. Determination of vortex parameters, (a) circulation and (b) swirl velocity.

encloses vorticity. The procedure of the “disk” method is to first integrate (both positive and negative) vorticity over areas within succeeding values of radius r , to render circulation Γ as a function of r . The result of this integration is shown in Fig. 15(a). Using the relationship $v = \Gamma/2\pi r$, one obtains Fig. 15(b), where r_C is chosen at the maximum value of v (designated as v_C , $v_C = \Gamma_C/2\pi r_C$). Here, this method gives $(r_C, v_C) = (.0143 \text{ m}, 4.9 \text{ m/s})$, which is deemed to be a more accurate measure of the vortex than that found above using the two cut procedure of Fig. 13(a) and then averaging the two results. The analytical curve in Fig. 15(b) is a calculated description of the velocity profile using a method to be described.

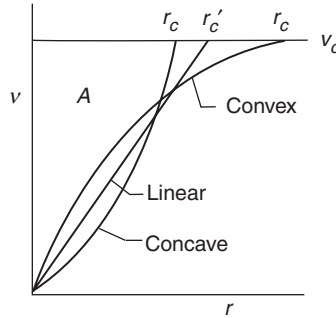


Figure 16. Types of velocity profile shapes.

Besides providing values of r_C and v_C , the disk method velocity profile in Fig. 15(b) can be presumed to be a good representation of that for the vortex. As a first step in quantifying the profile shape of the vortex core region, Fig. 16 illustrates several possible profile shapes within the core of a vortex. Convex, linear, and concave profiles are shown. If A in the figure is the area of velocity deficit, then $A = (1/2)r'_C v_C$, where r'_C is the Rankine (linear profile) vortex core radius with velocity v_C . In general, for the area

$$A = v_C r_C \int_0^1 (1 - v/v_C) d\tilde{r} \quad (2)$$

where $\tilde{r} = r/r_C$, so

$$r'_C/r_C = 2 \int_0^1 (1 - v/v_C) d\tilde{r} \quad (3)$$

The ratio r'_C/r_C is taken to be a “shape factor” of interest. When $r'_C/r_C < 1$ the profile is convex, when $r'_C/r_C = 1$ the profile is Rankine (linear), and when $r'_C/r_C > 1$ it is concave. Equation (3) is readily evaluated from processed v results, such as in Fig. 15(b). When $r'_C/r_C \leq 1$, we can choose an algebraic velocity-profile description to describe most of the profiles found in the present study. This is the Vatisas³⁹ profile, where the velocity is given by

$$v/v_C = 2^{1/n} \{ \tilde{r} / (1 + \tilde{r}^{2n}) \}^{1/n} \quad (4)$$

where within the vortex core, $\tilde{r} \leq 1$, and outside of the core, $\tilde{r} > 1$. The number $n = 1$ gives the Scully vortex model⁴⁰ shape, often used for rotorcraft vortex definitions⁴¹; and $n = 2$ gives a vortex description^{22,24} found to give good results for vortices measured for a model rotor in hover. The Rankine vortex model is obtained when $n = \infty$. Equation (4) does not provide a description for a convex profile. From Eqs. (3) and (4), one can

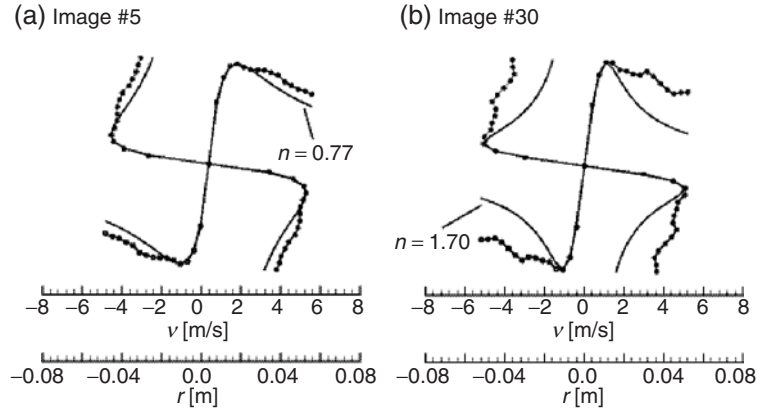


Figure 17. Velocity cut presentation of Disk method results to correspond to Fig. 13 (a) and (b).

relate values of n (such as .5, 1, 2, and ∞) to values of r'_C/r_C (.455, .614, .754, and 1, respectively).

The analytic curve of Fig. 15(b) is determined from Eq. (4), using the r_C , v_C , and n values found in the use of Eq. (3) with the data. The same image #5 results are presented in Fig. 17(a) in the swirl format of Fig. 13(a) for direct comparison with the velocity cuts. Also, Fig. 17(b) compares with Fig. 13(b) in the same way, but for image #30. Note that a very different value of n was found for this particular velocity profile.

It is important to note that emphasis is given in this paper to define velocity profile characteristics within the vortex core. In Fig. 17, the good agreement of Eq. (4) using the respective n values is not matched outside of the core. The n values in this equation determine how much of the circulation associated with the vortex is contained within the core (for the particular equation form). With Γ_C being the circulation within the core (as per the disk method, $v_C = \Gamma_C/2\pi r_C$) and $\Gamma_{TOT-Vortex}$ is the total circulation associated with the vortex, then

$$\Gamma_C = 2^{-1/n} \Gamma_{TOT-Vortex} \quad (5)$$

where for $n = 1, 2, \infty$, $2^{-1/n} = .5, .707, 1$. It is seen that because of Eq. (5), one could emphasize the outer velocity profile in determining n , to get better agreement there, but again the present purpose is to describe core region profile.

Figure 18 presents the analytic result for the same PIV cut plane #22 using average \bar{r}_C , \bar{v}_C , and \bar{n} values (.0183 m, 4.69 m/s, and .684, respectively). These were obtained from simple mean averaging of r_C and v_C , and for n , determined from corresponding mean values of r'_C/r_C . This result can be taken to represent the mean vortex of the PIV cut plane. The parameters r_C , v_C , and r'_C/r_C (not n) were found to have near normal statistical distributions. This averaging method gives less bias error than one involving

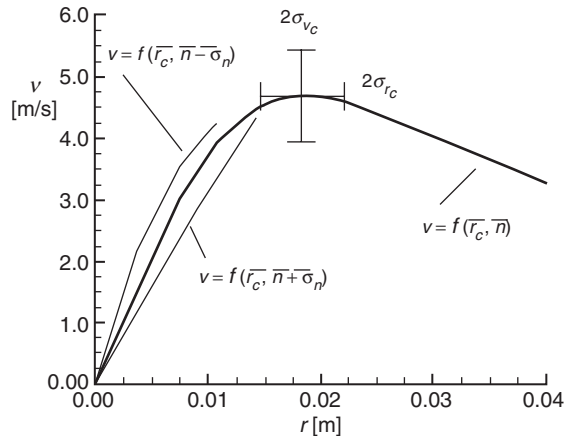


Figure 18. Mean vortex velocity profile for PIV cut plane #23, for $\alpha = 5.3^\circ$. Unsteadiness limits of instantaneous values are shown.

conditional averaging of profiles and then determining parameters (see previous section). To address unsteadiness (non-repeatability) questions for instantaneous images, Fig. 18 “unsteadiness” limits are shown that enclose the mean vortex velocity profile. The limits provide a measure of how well an instantaneous vortex is represented by the mean vortex. This is not an “error” band. The limits enclose curves determined when \bar{r}_C , \bar{v}_C , and \bar{n} are each independently varied about their standard deviations, $\pm \sigma_{r_C}$, $\pm \sigma_{v_C}$, and $\pm \sigma_n$ (determined from $r'_C/r_C \pm \sigma_{r'_C}/r_C$).

As mentioned, the above method assumes that the vortex axis (tube) is normal to the cut plane. As previously indicated, the vortices of this study can have tilt angle with respect to the normal on the order of 30° at the larger y_{TUN} value cut lines (outer part of rotor disk). This suggests possible local errors of $\pm 15\%$ in velocity and vortex dimensions. However, because of an averaging effect, the disk method for such a tilt amplitude should render a result for r_C that is about 7% too large and a result for v_C that is about 7% too small. Such errors should not affect the following parametric presentations significantly, but this should be kept in mind.

CV Criterion using Disk Method

The disk method is an objective means to determine vortex parameters. What it calculates depends on the choice of CV in the flow field. The use of the 80% criterion, CV_{80} , may correctly pinpoint the center of the dominant vortex within the image, or may locate a “false” location when the vortex is ill defined, such as when it’s weak, or it may identify a portion of a burst or fragmented vortex. In the latter case, the calculation may find a smaller vortex than it should. Such results for vortex radius, velocity, and shape factor would be averaged into the other image results to get a mean vortex. The use of the 20% criterion, CV_{20} , tends to find the group center of vorticity. Here the CV would generally be between areas of peak vorticity and thus would tend to

calculate a larger dispersed vortex. This may be appropriate for burst vortices, for example, but it may not be for a small vortex attached to a strong elongated shear layer. For well-defined vortices, the results for the different criteria should be very similar. This in itself makes comparison of results from the different criteria valuable.

Vortex Parameter Results

In this section, vortex parameters are examined over the wake for the baseline $\alpha = 5.3^\circ$ rotor condition and α variations. The normalized parameters are core radius \bar{r}_C/C , mean maximum spin velocity \bar{v}_C/V_T , velocity profile shape factor r'_C/r_C , and vortex wander δ/C (to be defined). Here, V_T is the rotor tip speed and C is the blade chord length. Many of these parameters are also listed in Table 1.

In the following parameter presentations for the baseline case, the results of both CV criteria are shown.

Advancing Side - Baseline Condition

Figures 19(a) and (b), using the CV_{20} and CV_{80} criteria, respectively, show parameter contours plotted over the rotor's advancing side. These are top views that show the rotor plane disk edge and rotor hub axis defined with respect to the tunnel coordinates x_{TUN} and y_{TUN} . The centers of the PIV image frames are shown as grid points for the data.

The different criteria are seen to give very similar results over much of the rotor disk, indicating that such vortices are well defined. As expected, based on the above discussions, the CV_{20} results have larger \bar{r}_C over regions where young vortices are forming and where the vortices are weak or fragmented. The CV_{80} results are taken as being more correct, based upon comparison with Fig. 5 and other data. The velocity contours show only a slight decrease with CV_{20} from those of CV_{80} . The shape factors show, in general, an increase due to CV_{20} locations being somewhat displaced from maximum vorticity locations. Here, the disk method would emphasize velocity growth at larger r values, thereby rendering more concave profile shapes. The wander δ of the CV position is seen to be less with CV_{20} . This indicates that, within each instantaneous image frame, the region of strong vorticity is more stable than the vortices themselves, whose instantaneous positions are better reflected by CV_{80} .

Upon accepting CV_{80} as giving more accurate parameters, it is seen that younger vortices (negative x_{TUN} near the rotor disk edge) start out at with radii \bar{r}_C of 5 to 10% of chord. The vortices, at mid y_{TUN} values, experience moderate radii growth to 10 to 15% of chord and then appear to start contracting. In Fig. 5, some tightening of the vortices are seen at positive x_{TUN} , but also the vortex experience splitting and the disk method with CV_{80} may have picked up on just one of the split vortices. The velocities \bar{v}_C undergo a slight drop after the vortex is formed and then remains stable.

Strong vortices are found near $\psi \approx 90^\circ$ ($y_{TUN} \approx 2.0$). As ψ approaches 180° ($y_{TUN} = 0$, x_{TUN} is negative), they weaken. This is anticipated from predictions^{13,14} and previous measurements for this rotor system⁹. The blades have high tip loading near $\psi \approx 90^\circ$ but reduce almost linearly to $\psi = 180^\circ$. The fact that \bar{r}_C and \bar{v}_C values remain almost

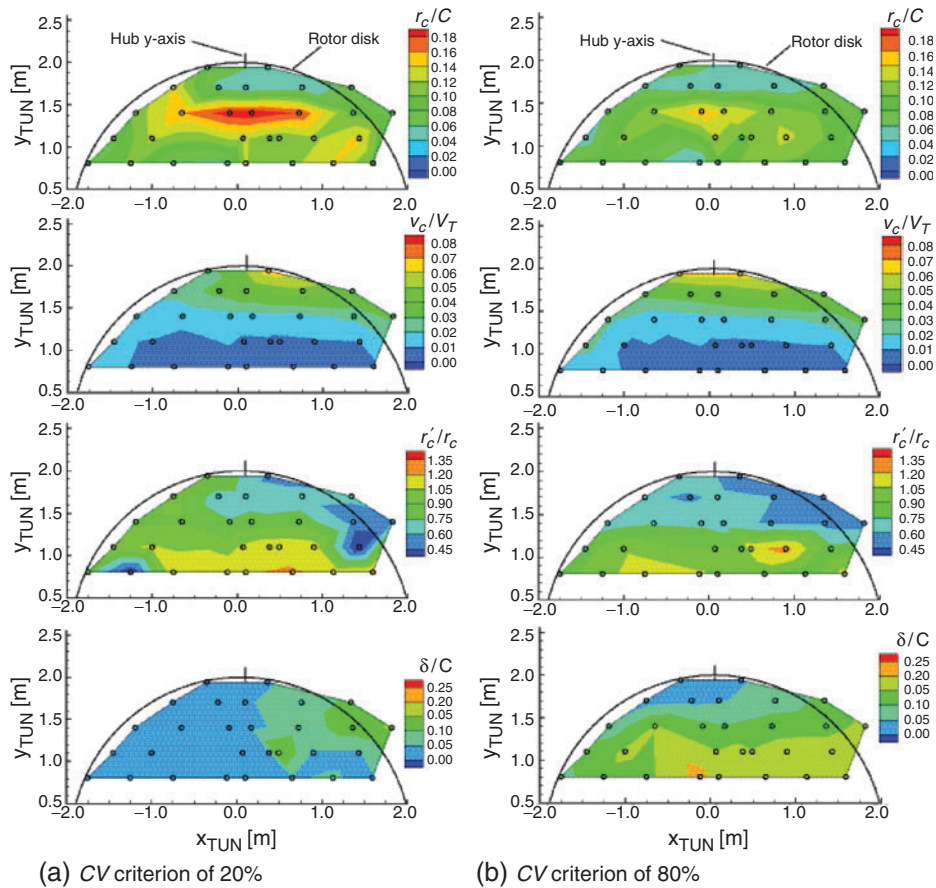


Figure 19. Advancing-side rotor disk distribution of normalized vortex parameters (baseline condition, $\alpha = 5.3^\circ$).

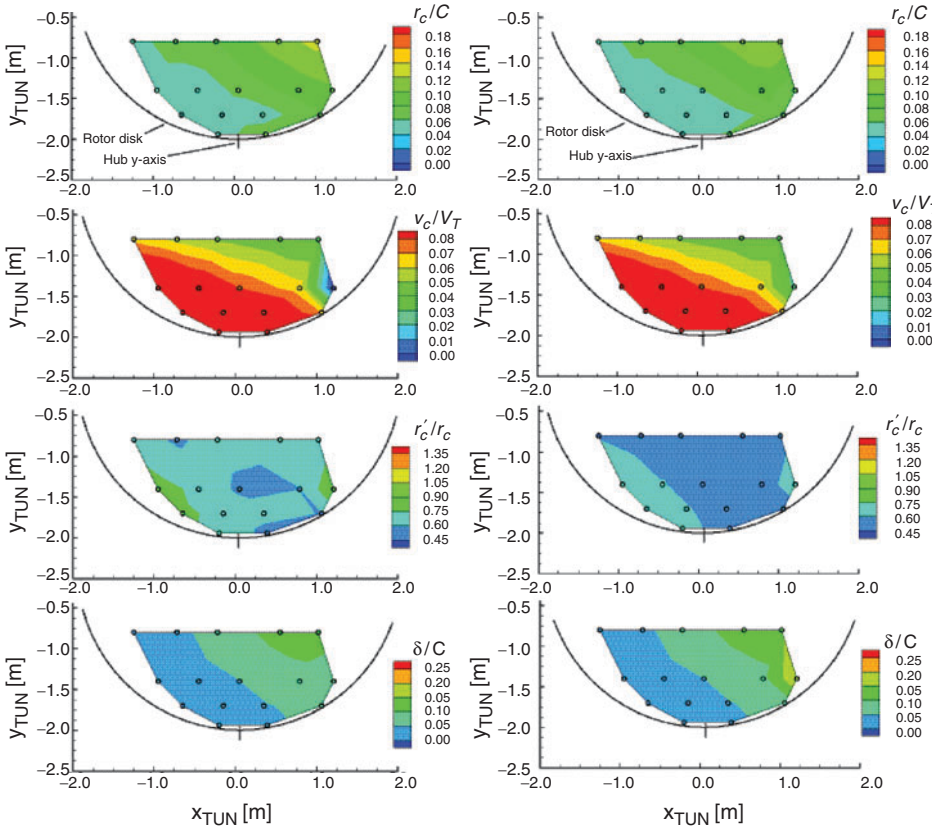
constant across much of x_{TUN} shows that once formed, the vortices are stable and generally maintain their strength. Although no detail comparative evaluation has been made, the present more-accurate PIV vortex measurements appear to find the vortices to be much smaller, about 40% of that found by the previous LDV measurements¹⁸ of this rotor. The data sampling for the LDV method in many respects duplicated the spatial averaging effects illustrated in the straight averaging approach of Fig. 12(c) of the present paper. For that illustration, the straight averaging approach produced a radius of about 38 mm, Ref. 9 found about 30 mm for a similar location in the wake, and the present disk method finds 14 mm.

Over most of the advancing side, where the shape factor $r'_c/r_c < 1$, the vortices have the traditional convex velocity profile shapes. For larger y_{TUN} values, the commonly assumed Scully shape ($r'_c/r_c \approx .61$, $n \approx 1$) and the more peaked profiles of $n \approx 2$

($\omega_z \approx .75$) are found. However, more inboard, very sharp profiles approaching the Rankine profile ($r'_c/r_c = 1$) are found.

The term δ represents the degree that vortices wander within the data set. It is simply defined as the average distance δ that a vortex, positioned at CV_j within an instantaneous image j , is from the mean vortex position, \overline{CV} , for that set of 100 images.

$$\delta = \frac{1}{j} \sum_j |CV_j - \overline{CV}| \quad (6)$$



(a) CV criterion of 20%

(b) CV criterion of 80%

Figure 20. Retreating-side rotor disk distribution in format of Fig. 19 (baseline condition, $\alpha = 5.3^\circ$).

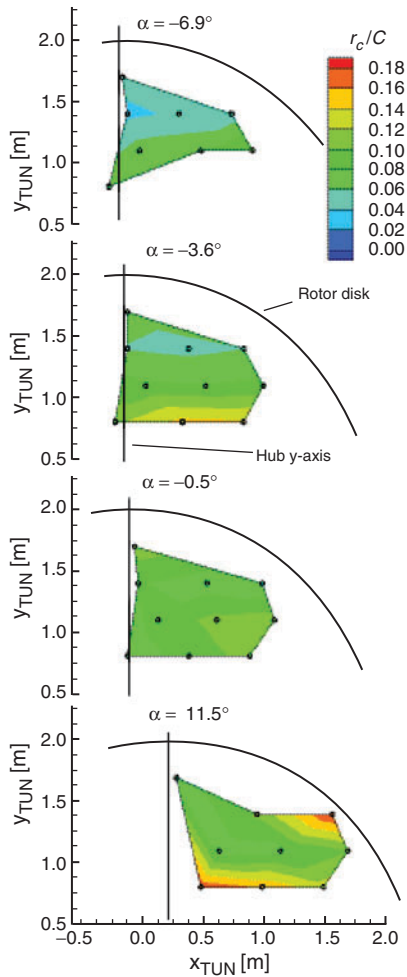


Figure 21. Core size variation due to rotor angle change. Advancing side. CV criterion of 80%.

It is seen in Fig. 19(b) that δ/C starts at negative x_{TUN} to be small and increases somewhat in the downstream direction. δ is larger (up to 20% chord) for weaker or disrupted vortices.

Retreating Side - Baseline Condition

Figures 20(a) and (b), for the retreating side, show that in most respects the results for both CV_{80} and CV_{20} are very similar, showing the vortices to be generally well defined. The very strong vortices in evidence are downstream of high blade tip loading as cited in Ref. 9 and 14 for this rotor. At younger stages, \bar{r}_C is small at about 4% of

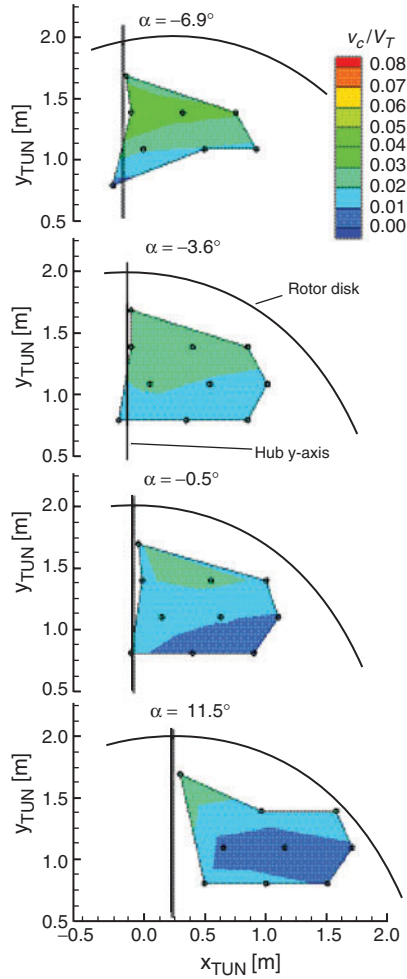


Figure 22. Swirl velocity variation due to rotor angle change. Advancing side. CV criterion of 80%.

chord length. Downstream, it appears to increase by a factor of 3. Swirl velocity correspondingly drops. This is in contrast to the advancing side where the (weaker) vortices appear to stabilize. The shape factor r'_c/r_c indicates that the velocity profiles fit the Scully or flatter (rounder) peak profile models. The wander δ is seen to be quite small for young vortices and progressively increase to about 15% of chord downstream.

Rotor Angle Variation - Advancing Side

For variation in rotor shaft angle, Figs. 21, 22, and 23 show the behaviors of \bar{r}_c/C , \bar{v}_c/V_T , and δ/C , respectively, over a portion of the first rotor quadrant. (One can

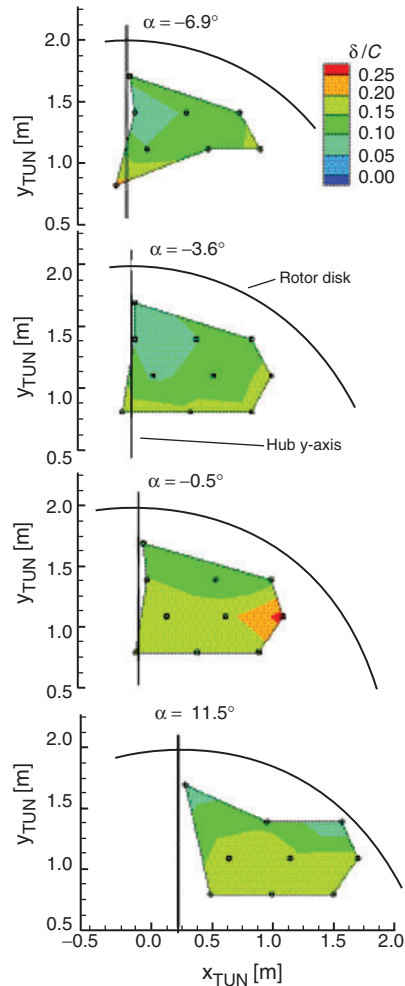


Figure 23. Vortex wander variation due to rotor angle change. Advancing side. CV criterion of 80%.

correspond the grid points across $y_{TUN} = 1.4$ m to image frames in Figs. 7, 8, 9, and 11.) As in Fig. 19, the centers of vorticity were chosen using the 80% criterion. The basic trends are, as the rotor condition changes from one of climb ($\alpha = -6.9^\circ$) to steep descent ($\alpha = 11.5^\circ$), that the vortex size increases on the order of 100%, the vortex swirl velocity decreases about 60%, and wander increases about 50%.

CONCLUSIONS

The 3-C PIV database from the HART II program, with detail flow information over the rotor disk for a rotor in forward flight, is unique and provides a means to evaluate and

develop improved wake codes. The present effort is a first in-depth analysis of the benchmark database. The present analysis provides substantial insight to the rotor wake's vortex structure.

Processing methods to define important vortex parameters from the PIV database were examined and a new method was developed and evaluated. Compared to commonly used vortex definition methods using velocity cuts of instantaneous and/or averaged (straight or conditionally) vortex velocity fields, the present center-of-vorticity criterion and vorticity "disk" integration method appears more objectively based and is robust.

Important determinations and confirmations for wake vortices were found. In general, previous predictions and measurements (by other, less accurate means) confirm the vortex strength dependence with blade tip loading. However, vortex core sizes are substantially smaller (~40% of previous values on the advancing side near BVI locations). Also, previous assumptions about core velocity profile-shape definitions (such as Scully's model) can be substantially in error. Large ranges of vortex velocity shapes exist over the rotor disk for this forward flight case. Unsteadiness or wander of vortex path starts out small at creation but grows to about 15 to 20% of the chord length.

ACKNOWLEDGEMENTS

An international test as complex as HART II requires a lot of engagement of all participants, both in the foreground and background. It would fill pages to name everybody. Instead, the teams are specifically addressed. These are the prediction team, the test team, and the management team, all consisting of US/French/German members working years ahead in real partnership. Specifically acknowledged is the funding of the test from the US and French side, the development of 3C-PIV, preparation of the rotor, and conduction of the test from the DLR side, and the strong testing support of DNW.

REFERENCES

1. Schmitz, F. H., "Rotor Noise", *Aeroacoustics of Flight Vehicles, Theory and Practice, Vol. 1, Noise Sources*, edited by H. H. Hubbard, Acoustical Society of America, New York, 1995, pp. 65-149.
2. Boxwell, D. a , Schmitz, F. H., Spletstoesser, W. R., Schultz, K. J., "Helicopter Model Rotor-Blade Vortex Interaction Impulsive Noise: Scalability and Parametric Variations," *Journal of American Helicopter Society*, vol. 32, No. 1, 1987.
3. Brooks, T. F., Booth, E.R., Spletstoesser, W. R., Schultz, K. J., Kube, R., Niesel, G., and Streby, O., "Analysis of a Higher Harmonic Control Test to Reduce Blade Vortex Interaction Noise," *Journal of Aircraft*, Vol. 31, No. 6, Nov-Dec 1994, pp. 1341-1349.
4. Spletstoesser, W. R., Schultz, K. J., Kube, R., Brooks, T. F., Booth, E. R., Niesel, G., and Streby, O., "BVI Impulsive Noise Reduction by Higher Harmonic Pitch Control: Results of a Scaled Model Rotor Experiment in the DNW," presented at the 17th European Rotorcraft Forum, September 24-26, 1991, Berlin, Germany.

5. Brooks, T. F., Burley, C. L., "Rotor Broadband Noise Prediction with Comparison to Model Data," AIAA Paper 01-2210, 7th AIAA/CEAS Aeroacoustics Conference, Maastricht, The Netherlands, May 2001.
6. Brezillon, J., Prieur, J., and Rahier, G., "Investigation on Broadband Helicopter Rotor Noise," AHS Technical Specialists' Meeting For Rotorcraft Acoustics and Aerodynamics, Williamsburg, Virginia, October 28-30, 1997.
7. Yu, Y. H., Gmelin, B., Heller, H., Philippe, J. J., Mercker, E., and Preisser, J. S., "HHC Aeroacoustics Rotor Test at the DNW - the Joint German/French/US HART project," 20th European Rotorcraft Forum, Amsterdam, Netherlands, 1994.
8. Kube R., Splettstoesser W. R., Wagner W., Seelhorst U., Yu Y. H., Boutier A., Prieur J., and Mercker E., "Initial Results from the Higher Harmonic Control Aeroacoustic Rotor Test (HART) in the German-Dutch Wind Tunnel," presented at the 75th AGARD Fluid Dynamics Panel Symposium on Aerodynamics and Acoustics of Rotorcraft, Berlin, Germany, 10-14 October 1994.
9. Splettstoesser, W. R., Kube, R., Wagner, W., Seelhorst, U., Boutier, A., Micheli, F., Mercker, E., Pengel, K., "Key Results from a Higher Harmonic Control Aeroacoustic Rotor Test (HART)," *Journal of the American Helicopter Society*, January 1997.
10. Mercker, E., Pengel, K., "Flow Visualization of Helicopter Blade-Tip Vortices – a qualitative Technique to Determine the Trajectory and the Position of the Tip Vortex Pattern of a Model Rotor," 18th European Rotorcraft Forum, Avignon, France, 1992.
11. Seelhorst, U., Butefisch, K. A., Sauerland, K. H., "Three Component Laser-Doppler Velocimeter Development for Large Wind Tunnel, ICIASF, 1993 Record, 1993.
12. Gallman, J. M., Tung, C., Schultz, K.-J., Splettstoesser, W., Buchholz, H., Spiegel, P., Burley, C. L., Brooks, T. F., and Boyd, D. D. Jr., "Effect of Wake Structure on Blade-Vortex Interaction Phenomena: Acoustic Prediction and Validation," 16th AIAA Aeroacoustic Conference, Munich, Germany, June 1995.
13. Tung, C., Gallman, J. M., Kube, R., Wagner, W., Van der Wall, B., Brooks, T. F., Burley, C. L., Boyd, D. D., Rahier, G., and Beaumier, P., "Prediction and Measurement of Blade-Vortex Interaction Loading," presented at the 1st Joint CEAS/AIAA Aeroacoustics Conference, Munich, Germany, June 12-15, 1995.
14. Brooks, T. F., Boyd, D. D., Burley, C. L., and Jolly, R. J., "Aeroacoustic Codes for Rotor Harmonic and BVI Noise-CAMRAD.Mod1/HIRES," *Journal of the American Helicopter Society*, pp. 63-79, Apr. 2000.
15. Costes, M., Beaumier, P., Bettschart, N., Coppens, G., and Servera, G., "Computational Tools Used At ONERA for the Description of Helicopter Rotor Wakes," AIAA Paper 00-0113, 38th Aerospace Sciences Meeting and Exhibit, Reno, NV 2000.
16. Lim, J.W., Tung, C., and Yu, Y.H., "Prediction of Blade-Vortex Interaction Airloads with Higher-Harmonic Pitch Controls Using the 2GCHAS Comprehensive Code," *Journal of Pressure Vessel Technology*, Transaction of the ASME, Vol. 123, No. 4, 2001.

17. Wachspress, D. A., Quackenbush, T. R., "BVI Noise Prediction Using a Comprehensive Rotorcraft Analysis," American Helicopter Society 57th Annual Forum, Washington, D. C., May 9-11, 2001.
18. van der Wall, B. G., "Vortex Characteristics Analysed From HART Data", European Rotorcraft Forum, Dresden, Germany, 1997.
19. Kube, R., and Schultz, K. J., "Vibration and BVI Noise Reduction by Active Rotor Control: HHC Compared to IBC." 22nd European Rotorcraft Forum, Brighton, UK, 1996.
20. Leishman, J. G., Baker, A., and Coyne, A. J., "Measurements of Rotor Tip Vorticities Using Three-Component Laser Doppler Velocimetry, *Journal of the American Helicopter Society*, Vol. 41, No. 4, 1996.
21. Leishman, J. G., "Measurements of the Aperiodic Wake of a Hovering Rotor," *Experiments in Fluids*, vol. 25, No. 4, 1998, pp. 352-361.
22. Han, Y. O., Leishman, J. G., and Coyne, A. J., "Measurement of the Velocity and Turbulence Structure of a Rotor Tip Vortex," *AIAA Journal*, Vol. 35, No. 3, March 1997.
23. Coyne, A. J., Ghagwat, M. J., Leishman, J. G., "Investigation into the Rollup and Diffusion of Rotor Tip Vortices Using Laser Doppler Velocimetry," 53rd Annual American Helicopter Society Forum, May 1997.
24. Bhagwat, M. J., Leishman, J. G., "Generalized Viscous Vortex Model for Application to Free-Vortex Wake and Aeroacoustic Calculations," American Helicopter Society 58th Annual Forum, Montreal, Canada, June 11-13, 2002.
25. Bhagwat, M. J., Leishman, J. G., "Correlation of Helicopter Rotor Tip Vortex Measurements," *AIAA Journal*, Vol. 38, No. 2, 2000, pp. 301-308.
26. Martin, P. B., Pugliese, G. J., and Leishman, J. G., "High Resolution Trailing Vortex Measurements in the Wake of a Hovering Rotor," American Helicopter Society 57th Annual Forum, Washington, D.C., May 9-11, 2001.
27. Martin, P. B., Leishman, J. G., "Trailing Vortex Measurements in the Wake of A Hovering Rotor Blade with Various Tip Shapes," American Helicopter Society 58th Annual Forum, Montreal, Canada, June 11-13, 2002.
28. Heineck, J. T., Yamauchi, G. K., Wadcock, A. J., Lourenco, L., and Abrego, A. I., "Application of Three-Component PIV to a Hovering Rotor Wake," American Helicopter Society 56th Annual Forum, Virginia Beach, Virginia, May 2-4, 2000.
29. McAlister, K. W., Tung, C., and Heineck, J. T., "Forced Diffusion of Trailing Vorticity From a Hovering Rotor," American Helicopter Society 57th Annual Forum, Washington, D.C., May 9-11, 2001.
30. Raffel, M., Seelhorst, U., and Willert, C., "Vortical Flow Structures at a Helicopter Rotor Model Measured by LDV and PIV," *The Aeronautical Journal*, Paper No. 2227, April 1998.
31. Murashige, A., Tsuchihashi, A., Tsujiuchi, T., and Yamakawa, E., "Blade-tip vortex Measurement by PIV, Proc of the 23rd European Rotorcraft Forum, Paper 36, Dresden, Germany, 1997.

32. Yamauchi, G. K., Burley, C. L., Mercker, E., Pengel, K., and JanakiRam, R., "Flow Measurements of an Isolated Model Tilt Rotor," American Helicopter Society 55th Annual Forum, Montreal, Canada, May 25-27, 1999.
33. Yu, Y. H., Tung, C., van der Wall, B. G., Pausder, J., Burley, C. L., Brooks, T. F., Beaumier, P., Delrieux, Y., Mercker, E., and Pengel, K., "The HART-II Test: Rotor Wakes and Aeroacoustics with Higher-Harmonic Pitch Control (HHC) Inputs – The Joint German/French/Dutch/US Project", American Helicopter Society 58th Annual Forum, Montreal, Canada, May 25-27, 2002.
34. Raffel, M., Richard, H., Schneider, G., Klinge, F., Ehrenfried, K., Pengel, K., and Geenstra, G., "Recording and Evaluation Methods of PIV Investigations on a Helicopter Rotor Model," 11th International Symposium on Applications of Laser Techniques to Fluid Mechanics, Lisbon, 8-11 July, 2002.
35. Richard, H., Raffel, M., "Rotor Wake Measurements: Full-scale and Model Tests," American Helicopter Society 58th Annual Forum, Montreal, Canada, May 25-27, 2002.
36. van der Wall, B. G., Junker, B., Burley, C. L., Brooks, T. F., Yu, Y., Tung, C., Raffel, M., Hugues, R., Wagner, W., Mercker, E., Penge., K., Holthusen, H., Beaumier, P., and Delrieux, Y., "The HART II Test in the LLF of the DNW – A Major Step Towards Rotor Wake Understanding," 28th European Rotorcraft Forum, Bristol, England, September, 17-20, 2002.
37. Hart, D. P., "PIV Error Correction," *Experiments in Fluids*, Vol. 29, No. 1, 2000.
38. Raffel, M., Willert, C., Kompenhans, J., *Particle Image Velocimetry, A practical Guide*, Springer, ISBN 3-540-63683-8, 1998.
39. Vatistas, G. H., Kozel, V., Mih, W. C., "A Simpler Model For Concentrated Vortices," *Experiments in Fluids*, vol. 11, 1991.
40. Scully, M. P., "Computation of Helicopter Rotor Wake Geometry and Its Influence on Rotor Harmonic Airloads," Massachusetts Institute of Technology, ASRL TR 178-1, Mar. 1975.
41. Johnson, W., *Helicopter Theory*, Princeton Univ. Press, 1980.

APPENDIX

Table 1. Wake vortex parameter definitions for 80% CV criterion

α (deg)	cut #	nominal			wake age (deg)	r_c/C	$\sigma_{r_c/C}$	v_c/V_T	σ_{v_c/V_T}	r'_c/r_c	$\sigma_{r'_c/r_c}$	x_{cv} (cm)	y_{cv} (cm)	δ/C	$\sigma_{\delta/C}$	w_0 (m/s)	σ_{w_0} (m/s)	v_0 (m/s)	σ_{v_0} (m/s)	w_0 (m/s)	σ_{w_0} (m/s)
		x_{tun} (m)	y_{tun} (m)	z_{tun} (m)																	
5.3	29	-0.351	1.941	1.03	12	0.070	0.0899	0.0641	0.01073	0.65	0.770	-1.20923	0.21517	0.171	0.0247	-27.9	3.97	3.9	0.57	16.6	2.36
5.3	30	0.359	1.941	1.06	102	0.050	0.0571	0.0644	0.00275	0.50	0.567	-1.59805	0.50836	0.173	0.0236	-30.0	6.04	0.2	0.27	13.2	2.67
5.3	24	-0.75	1.701	1.1	45	0.050	0.0707	0.0337	0.00619	0.59	0.691	-0.36362	1.20374	0.169	0.0222	-28.1	3.99	3.1	0.47	16.7	2.38
5.3	25	-0.221	1.701	1.12	135	0.044	0.0566	0.0360	0.00454	0.52	0.606	0.95036	0.70545	0.170	0.0263	-30.4	4.33	1.4	0.30	15.8	2.25
5.3	26	0.099	1.701	1.1	175	0.039	0.0455	0.0399	0.00335	0.56	0.635	-0.31475	1.09655	0.172	0.0331	-30.8	4.39	-2.1	0.44	14.7	2.09
5.3	27	0.759	1.701	1.04	265	0.043	0.0488	0.0462	0.00353	0.57	0.640	-0.27534	-0.27215	0.183	0.0500	-31.9	4.54	-6.3	0.98	13.6	1.97
5.3	28	1.339	1.701	0.92	355	0.061	0.0822	0.0422	0.00390	0.53	0.604	1.68181	-0.04194	0.198	0.0699	-29.3	4.20	-8.1	1.24	14.1	2.06
5.3	17	-1.19	1.401	1.14	30	0.094	0.1371	0.0108	0.00358	0.82	1.011	-0.63929	0.85967	0.180	0.0589	-28.7	0.11	3.3	0.14	17.4	0.13
5.3	18	-1.425	1.401	1.14	120	0.092	0.1590	0.0083	0.00569	0.94	2.044	0.12073	2.44094	0.212	0.1328	-30.0	0.19	1.6	0.18	16.6	0.13
5.3	19	-0.091	1.401	1.16	210	0.105	0.1613	0.0119	0.00550	0.72	0.957	0.49758	0.02868	0.190	0.0937	-32.2	0.25	-1.0	0.36	15.6	0.18
5.3	21	0.725	1.401	1.04	313	0.109	0.1547	0.0172	0.00317	0.58	0.673	2.42117	-0.33911	0.198	0.0810	-32.2	0.43	-6.2	0.47	14.8	0.32
5.3	22	1.359	1.401	0.88	403	0.092	0.1270	0.0228	0.00266	0.54	0.630	0.06558	-0.03817	0.207	0.0782	-30.1	0.55	-9.3	0.53	14.5	0.39
5.3	23	1.819	1.401	0.77	493	0.062	0.0810	0.0345	0.00422	0.53	0.604	1.80369	0.32199	0.230	0.1016	-28.1	4.07	-5.9	1.08	15.6	2.28
5.3	9	-1.45	1.101	1.14	15	0.049	0.0789	0.0193	0.01239	0.84	1.155	-4.80586	2.60070	0.210	0.1235	-27.9	0.12	2.7	0.17	16.7	0.10
5.3	10	-1	1.101	1.2	105	0.080	0.1334	0.0060	0.00413	0.96	1.407	-1.10677	0.84934	0.226	0.1127	-31.1	0.12	1.8	0.21	16.6	0.12
5.3	11	0.491	1.101	1.2	195	0.075	0.1353	0.0041	0.00367	0.97	2.562	1.44370	1.22083	0.220	0.1068	-31.9	0.18	-0.3	0.30	16.4	0.19
5.3	12	0.069	1.101	1.13	285	0.085	0.1478	0.0044	0.00335	1.01	1.765	-0.04373	2.37849	0.217	0.1212	-31.3	0.30	-2.9	0.40	16.3	0.20
5.3	13	0.379	1.101	1.09	325	0.066	0.1114	0.0034	0.00275	1.17	2.357	-1.75157	1.84935	0.226	0.1424	-31.8	0.34	-6.3	0.64	18.0	0.28
5.3	14	0.899	1.101	0.97	415	0.078	0.1380	0.0036	0.00289	0.89	3.182	-0.66891	1.96289	0.244	0.1148	-31.1	0.42	-7.8	0.69	17.7	0.42
5.3	15	1.429	1.101	0.83	505	0.076	0.1331	0.0050	0.00482	0.72	2.876	-2.18886	-1.45630	0.238	0.1145	-29.9	0.59	-9.5	0.55	16.7	0.45
5.3	1	-1.75	0.806	1.17	5	0.067	0.1083	0.0146	0.00936	0.67	2.304	0.49723	0.62719	0.188	0.0556	-28.9	0.10	2.7	0.12	16.8	0.13
5.3	2	-1.25	0.806	1.21	95	0.071	0.1232	0.0075	0.00550	0.83	1.908	0.77855	1.59065	0.212	0.1023	-30.6	0.15	1.8	0.20	16.8	0.18
5.3	3	-0.75	0.806	1.21	185	0.050	0.0855	0.0040	0.00335	1.67	5.981	2.59484	2.09895	0.209	0.0991	-31.2	0.18	0.2	0.20	17.2	0.18
5.3	4	-0.116	0.806	1.15	275	0.037	0.0709	0.0040	0.00271	1.09	2.804	-0.48157	1.45378	0.266	0.1645	-30.9	0.31	-3.3	0.51	16.8	0.25
5.3	5	0.099	0.806	1.15	315	0.067	0.1242	0.0034	0.00280	0.94	1.1262	-0.72645	1.72275	0.233	0.1136	-30.9	0.40	-5.6	0.62	17.4	0.28
5.3	6	0.649	0.806	1.05	405	0.056	0.0962	0.0031	0.00220	0.91	1.556	-1.79914	1.29922	0.237	0.1266	-31.0	0.37	-7.4	0.78	16.6	0.34
5.3	7	1.129	0.806	0.9	495	0.066	0.1254	0.0031	0.00326	1.09	2.593	-0.65177	1.08233	0.246	0.1388	-29.2	0.50	-8.1	0.90	16.2	0.51
5.3	8	1.589	0.806	0.76	585	0.063	0.1024	0.0048	0.00358	-0.73	14.458	1.24439	-1.32681	0.270	0.1185	-27.5	0.59	-10.2	0.49	15.6	0.43
5.3	31	-1.249	-0.8	1.21	77	0.071	0.1384	-0.0128	0.01972	0.90	1.085	-0.12497	0.74332	0.168	0.0191	30.3	0.16	4.4	0.18	18.2	0.08
5.3	32	-0.719	-0.8	1.2	167	0.049	0.1031	-0.0062	0.01376	0.93	1.140	-1.44455	0.77977	0.171	0.0296	31.1	0.25	-1.3	0.33	19.5	0.14
5.3	33	-0.22	-0.8	1.16	257	0.058	0.1221	-0.0077	0.01436	0.95	1.188	-1.24039	0.49378	0.178	0.0508	30.7	0.39	-4.4	0.46	19.7	0.21
5.3	34	0.55	-0.8	1.07	397	0.064	0.1337	-0.0061	0.01183	0.88	1.085	-1.58907	0.62265	0.207	0.0735	30.4	0.71	-6.4	0.82	19.3	0.36
5.3	35	1.02	-0.8	0.98	487	0.074	0.1452	-0.0092	0.01436	0.88	1.136	-0.56147	0.80282	0.215	0.0913	29.7	0.81	-8.7	0.93	18.2	0.48
5.3	43	-0.949	-1.4	1.15	48	0.050	0.0544	-0.1129	0.00335	0.66	0.722	-0.92113	0.86664	0.168	0.0171	31.1	0.20	1.3	0.19	18.2	0.13
5.3	44	-0.45	-1.4	1.13	139	0.049	0.0540	-0.0965	0.00257	0.59	0.659	-0.28498	0.97827	0.170	0.0275	31.3	0.31	-3.0	0.30	19.1	0.16
5.3	45	0.05	-1.4	1.08	229	0.059	0.0671	-0.0794	0.00266	0.53	0.596	-0.41460	0.78189	0.172	0.0405	30.8	0.46	-6.5	0.35	19.6	0.21
5.3	46	0.79	-1.4	0.93	368	0.086	0.1000	-0.0632	0.00248	0.52	0.590	-0.90620	0.26189	0.186	0.0475	29.3	0.67	-8.8	0.66	19.8	0.41
5.3	47	1.21	-1.4	0.84	499	0.064	0.0899	-0.0237	0.01661	0.68	0.845	-0.30343	0.71981	0.236	0.1695	30.2	0.63	-10.2	0.35	19.2	0.31
5.3	48	-0.649	-1.7	1.12	42	0.088	0.1587	-0.0386	0.04165	0.97	1.211	-0.90030	-0.14458	0.168	0.0222	32.5	0.24	0.8	0.24	16.9	0.18
5.3	49	-0.15	-1.7	1.09	132	0.074	0.1430	-0.0292	0.03734	0.99	1.179	-0.15095	0.94508	0.170	0.0303	31.9	0.43	-4.1	0.34	18.5	0.29
5.3	50	0.35	-1.7	1.03	222	0.047	0.1089	-0.0082	0.02110	0.90	1.119	0.21533	0.12322	0.173	0.0335	32.3	0.44	-8.3	0.43	18.6	0.41
5.3	51	1.06	-1.7	0.87	362	0.063	0.0828	0.0321	0.00771	0.61	0.716	-0.33265	0.37080	0.183	0.0320	31.5	0.51	-9.8	0.35	19.7	0.60
5.3	52	-0.2	-1.94	1.06	27	0.076	0.1432	-0.0507	0.05624	0.92	1.101	-0.31947	0.32838	0.168	0.0201	32.3	0.38	1.7	0.23	15.8	0.27
5.3	53	0.39	-1.94	1.05	117	0.054	0.1086	-0.0193	0.04096	0.90	1.110	0.47297	0.49498	0.171	0.0310	35.5	0.47	-2.7	0.56	13.1	0.55
-6.9	26	-0.141	1.701	0.91	175	0.054	0.0934	0.0255	0.01239	0.71	1.857	-1.41006	0.34435	0.210	0.0546	0.0	0.22	-2.9	0.19	15.8	0.17
-6.9	20	-0.10	1.40	0.90	250	0.038	0.0442	0.0446	0.00606	0.62	0.702	-1.73476	-0.91151	0.174	0.0372	0.0	0.35	-5.7	0.34	15.7	0.17
-6.9	21	0.319	1.401	0.73	327	0.044	0.0540	0.0340	0.00518	0.61	0.695	0.04477	-0.26197	0.191	0.0812	0.0	0.67	-6.2	0.54	17.5	0.36
-6.9	22	0.7	1.40	0.73	417	0.046	0.0607	0.0318	0.00399	0.63	0.712	-0.42558	0.71118	0.216	0.0905	0.0	0.74	-6.2	0.68	18.8	0.45
-6.9	13	-0.001	1.101	0.7	325	0.062	0.0931	0.0213	0.00569	0.65	0.773	1.08862	1.21543	0.191	0.1080	0.0	0.53	-5.8	0.43	16.5	0.34
-6.9	14	0.499	1.101	0.7	415	0.064	0.0897	0.0195	0.00564	0.61	0.883	-1.09532	1.87425	0.199	0.0825	0.0	0.58	-6.9	0.55	16.7	0.38
-6.9	15	0.919	1.101	0.7	505	0.078	0.1235	0.0161	0.00743	0.69	0.868	1.52033	0.96669	0.230	0.0892	0.0	0.70	-6.8	0.69	17.3	0.48
-6.9	5	-0.251	0.806	0.9	315	0.035	0.0618	0.0031	0.00275	1.04	2.328	-0.62258	1.17737	0.272	0.1514	0.0	0.62	-5.2	0.41	16.7	0.28
-3.6	26	-0.101	1.701	0.96	175	0.061	0.0935	0.0296	0.00647	0.59	0.730	-1.96271	0.49896	0.191	0.0625	-29.7	0.34	-2.3	0.27	14.9	0.20
-3.6	20	-0.101	1.401	0.9	246	0.057	0.0815	0.0261	0.01211	0.72	1.003	-0.10758	1.55098	0.201	0.0363	-29.0	0.36	-4.3	0.30	15.0	0.20
-3.6	21	0.399	1.401	0.82	336	0.050															